

1 **Wind limits on stable rain layers and diurnal warm layers observed throughout the MJO**

2
3 Elizabeth J. Thompson¹, James N. Moum², Christopher W. Fairall³, Steven A. Rutledge⁴

4
5 ¹ Applied Physics Laboratory, University of Washington, Seattle, WA

6 ² College of Earth, Ocean, and Atmospheric Sciences, Oregon State University, Corvallis, OR

7 ³ NOAA/Earth Systems Research Laboratory, Boulder, CO

8 ⁴ Department of Atmospheric Science, Colorado State University, Fort Collins, CO

9
10 Submitted to the
11 *Journal of Geophysical Research - Oceans*
12 2 May 2018
13 Revised 15 Aug 2018
14

15 **Key Points:**

- 16 • Rain layers formed and persisted at higher wind speeds ($U_{10} \leq 9.8 \text{ m s}^{-1}$) compared to diurnal
17 warm layers ($U_{10} \leq 7.6 \text{ m s}^{-1}$)
18 • Stable layer formation and persistence above 5 m depth was well-estimated by U_{10} and the
19 surface buoyancy flux, B
20 • Rain layers (and their combinations with diurnal warm layers) formed often in disturbed and
21 active MJO periods before westerly wind bursts

22
23
24 Corresponding author address:
25 Elizabeth J. Thompson, Applied Physics Laboratory at the University of Washington
26 1013 NE 40th Street, Seattle, WA, 98102-6698
27 eliz@apl.uw.edu

28

ABSTRACT

29 Near-surface ocean stratification limits the penetration depth of wind-mixing and the
30 vertical distribution of atmospheric fluxes. Ship-based measurements from the central Indian
31 Ocean collected during the DYNAMO experiment indicate that significant density stratification
32 in the upper 5 m of the ocean was observed 38% of the time throughout two Madden-Julian
33 Oscillation (MJO) cycles. Stratification was caused by solar heating for diurnal warm layers
34 (DWLs, 30% of dataset), rainfall for rain layers (RLs, 16% of dataset), and both factors for their
35 combinations (RL-DWLs, 9% of dataset). RLs formed and persisted during higher wind ($U_{10} \leq$
36 9.8 m s^{-1}) than DWLs ($U_{10} \leq 7.6 \text{ m s}^{-1}$). RLs were rare and DWLs occurred nearly every day in
37 suppressed MJO periods, when $U_{10} \leq 8 \text{ m s}^{-1}$ and solar insolation was strong. During disturbed
38 and active MJO periods, which featured rain, increased cloudiness, and light winds ($U_{10} \leq 8 \text{ m s}^{-1}$),
39 RLs and RL-DWLs formed multiple times each day and individual DWLs waned in
40 frequency. Despite steady rainfall during westerly wind bursts, RLs rarely formed due to U_{10}
41 between 7-17 m s^{-1} .

42 From the ocean friction velocity, u_{w*} , and buoyancy flux, B , we derived estimates of \hat{h}_S ,
43 stable layer depth, and \hat{U}_S , the maximum U_{10} for which stratification should persist at \hat{h}_S for
44 fixed B . These estimates predicted 36 out of 44 observed stratification events within their
45 lifetimes (88% success rate), and predicted their wind limits. Therefore, U_{10} and B can be used to
46 predict ocean stable layer occurrence above 5 m.

47 **Plain Language Summary**

48 We found that rainfall and clear skies often led to stabilization of the upper 5 m of the
49 central Indian Ocean, except during strong winds. Near-surface stable layers impact the density
50 and mixing of the ocean because rain water and near-surface water heated by the sun are lighter
51 than typical ocean water, which is relatively cooler and saltier. Stable layers are important to
52 understand because they influence sea surface temperature and ocean heat content, which impact
53 weather and climate. Compared to previous studies, we more precisely determined the wind
54 speed below which stable layers form and above which they do not. This will hopefully aid
55 researchers and forecasters tasked with predicting tropical weather, climate, and ocean processes.

56 Prior to this study, it was unclear how often ocean stable layers formed during each phase
57 of the MJO, a major tropical phenomenon that impacts weather and climate around the world.
58 We found that stable rain layers (and their combinations with diurnal warm layers) occurred
59 most often in the later stages of the MJO, in its disturbed and active periods prior to wind bursts.
60 Diurnal warm layers tended to form in earlier stages of the MJO, in its suppressed and disturbed
61 periods.

62 1. Background and Motivation

63 Near-surface ocean stabilization can be achieved by either heat or freshwater inputs,
64 which suppress subsurface mixing and confine subsequent surface inputs of heat, momentum,
65 and freshwater to a shallow near-surface layer (*Miller 1976, Price 1979, You 1995, Soloviev and*
66 *Vershinsky 1982, Fairall et al. 1996a, Soloviev and Lukas 1996, 1997, 2006, Anderson et al.*
67 *1996, Smyth et al. 1996a, b, Wijesekera and Gregg 1996, Wijesekera et al. 1999, Asher et al.*
68 *2014, Drushka et al. 2016*). Near-surface stable layers can in turn impact sea surface temperature
69 and salinity (SST, SSS). Thermal stratification produces diurnal warm layers (DWLs) and
70 freshwater stratification produces rain layers (RLs). RLs occur often in tropical oceans where
71 precipitation is high and wind speeds are relatively low (*Lukas and Lindstrom 1991, Drushka et*
72 *al. 2016*). However, the wind limits on RLs and the prevalence of RLs throughout the lifecycle
73 of the Madden-Julian Oscillation (MJO) are unreported. On 30- to 60-day time scales, the MJO
74 explains the majority of variance in tropical net heat flux, wind, sea surface temperature (SST),
75 and rainfall (*Zhang 2005, Lau and Waliser 2005, de Szoeke et al. 2014, DeMott et al. 2015*). In
76 contrast to RLs, numerous previous studies report on DWL persistence and DWL occurrence
77 relative to MJO phase (*Price et al. 1986, Webster et al. 1996, Soloviev and Lukas 2006, Kawai*
78 *and Wada 2007, Bellenger and Duvel 2009, Matthews et al. 2014, Asher et al. 2014*). DWLs
79 form in response to absorption of shortwave solar radiation within the upper few meters of the
80 ocean. They have been observed when the 10-m level reference wind speed corrected for
81 neutrally-buoyant conditions, $U_{10, \leq 7 \text{ m s}^{-1}}$. The suppressed MJO period is characterized by
82 conditions of strong solar insolation and low wind speed, so DWLs are frequently observed to
83 form during this time. Unlike DWLs, the degree to which RLs and RL-DWL combinations can

84 withstand turbulent mixing by wind, and their resulting occurrence throughout the MJO, remains
85 unclear (*Lombardo and Gregg 1989, Brainerd and Gregg 1995, 1997, Price et al. 1986*).

86 Understanding the role of wind-forced mixing in the formation and evolution of RLs,
87 DWLs, and RL-DWL combinations is important for predicting SST. When DWLs and RLs are
88 present, surface inputs of momentum, heat, and freshwater are confined to shallow near-surface
89 layers. Daytime SST anomalies in DWLs can reach at least 4°C according to previous studies
90 (*Fairall et al. 1996a, Soloviev and Lukas 1997, Wijesekera et al. 1999, Woolnough et al. 2000,*
91 *Lau and Waliser 2005, Ward 2006, Drushka et al. 2012, Matthews et al. 2014, Soloviev and*
92 *Lukas 2006, Bellenger and Duvel 2009, Reverdin et al. 2012, Seo et al. 2014, DeMott et al.*
93 *2015*). In comparison, the intraseasonal variation in daily-mean SST is typically only 1°C (*Lau*
94 *and Waliser 2005, Demott et al. 2015*).

95 The demonstrated impact of stable layers on SST is relevant in determining air-sea
96 interaction and atmospheric convection. SST impacts the latent, sensible, and radiative heat
97 fluxes and the buoyancy flux into the atmosphere. These fluxes affect atmospheric boundary
98 layer circulation by generating buoyant convective motion and subsequent air pressure
99 adjustments (*Lindzen and Nigam 1987, Fairall et al. 1996a, Soloviev and Lukas 1997,*
100 *Woolnough et al. 2000, 2001, Costa et al. 2001, Back and Bretherton et al. 2009a, 2009b,*
101 *Bellenger et al. 2010, Clayson and Bogdanoff 2013, Seo et al. 2014, de Szoeke et al. 2014,*
102 *Ruppert and Johnson 2015, 206, Johnson and Ciesielski 2017*). Lateral SST gradients also lead
103 to the initiation and invigoration of precipitation due to air pressure adjustments and low-level
104 horizontal convergence (*Li and Carbone 2012, Carbone and Li 2015*).

105 Due to the impact of SST on atmospheric convection, both free-running and hindcast
106 general circulation models produce improved MJO simulations when air-sea coupling is included

107 in more detail, e.g. with hourly-averaged surface heat fluxes using a 1- or 3- dimensional (-D)
108 ocean model (*Bernie et al. 2005, 2007, 2008, Stan et al. 2010, Klingaman et al. 2011, Klingaman*
109 *and Woolnough 2014, Seo et al. 2014, DeMott et al. 2014, 2015, 2016, and references therein,*
110 *Chen et al. 2015*). Improved MJO fidelity in general circulation models improves accuracy in
111 predicting global weather and climate (*Lin et al. 2006, Hung et al. 2013, Zhang 2013*).

112 Parameterizations of ocean surface stratification by rain and diurnal warming are
113 necessary in coupled models concerned with accurate prediction of SSS and SST. DWL
114 parameterizations and 1-D ocean mixing models can reproduce observations of ocean
115 thermohaline structure when horizontal advection, underlying barrier layers, and other vertical
116 processes are not dominant factors (*Price et al. 1986, Fairall et al. 1996a*). For example, the
117 Rain Impact Model (RIM) provides a macro (i.e. 100 km) scale parameterization of rain's impact
118 on the ocean. However, RIM still requires testing with finer-scale observations of in-situ U_{10} and
119 rain rate, R (*Santos-Garcia et al. 2014*) and so far does not include DWLs.

120 Despite the importance of stably-stratified surface layers in controlling SST, near-surface
121 ocean stratification is not routinely observed. Owing to their shallow depth (typically less than a
122 few meters), DWLs and RLs are not detected by moorings without sensors in the upper 2 meters
123 (*Prytherch et al. 2013*). Similarly, Argo floats, expendable bathythermograph (XBT), and many
124 ship-based measurements often do not provide data within the first few meters of the ocean
125 surface and provide limited temporal and spatial coverage (*Anderson and Riser 2014, Chi et al.*
126 *2014, Asher et al. 2014*). Therefore, mixed layer depth climatologies developed using these data
127 describe the regional, monthly, nighttime, or daily-mean mixed layer depth, which is typically
128 10-30 m in the central Indian Ocean and varies by ± 15 m throughout an MJO cycle (*de Boyer*
129 *Montegut 2004, Schmidtko et al. 2013, Drushka et al. 2012, DeMott et al. 2015, Holte et al.*

130 2017). Climatologies developed using Argo data focus on mixed layer depth variability over time
131 scales on the order of one to two days since Argo data do not sample fast enough nor with
132 sufficient vertical resolution near the sea surface to resolve diurnal or sub-diurnal processes in
133 the upper 10 m.

134 Both Argo profiles and satellite overpasses are too infrequent relative to rain events to
135 characterize the occurrence rate of RLs and RL-DWLs, or to determine their sensitivity to U_{10} .
136 To some extent, the presence of RLs and DWLs can be detected by comparing the upper-most
137 Argo or mooring measurements of S and T with satellite-derived SSS or SST (*Kawai and Wada*
138 *2007, Boutin et al. 2013, Anderson and Riser 2014, Drushka et al. 2016*). However,
139 scatterometer- and radiometer-based measurements of U_{10} , SSS, and SST are contaminated by
140 precipitation and their 25-100 km scale footprints can also be too coarse spatially and temporally
141 (e.g. updating only a few times per day) to resolve the atmospheric mesoscale footprint of rain
142 (*Kummerow 2003, Kilpatrick et al. 2015*).

143 Ship observations have detected stable near-surface salinity gradients generated by rain
144 for a range of rain rates so long as $U_{10} < 9.5 \text{ m s}^{-1}$ (*You 1995, Soloviev and Lukas 1997,*
145 *Anderson et al. 1996, Smyth et al. 1996a, b, Wijesekera and Gregg 1996, Wijesekera et al. 1999,*
146 *Cronin and McPhaden 1999, Asher et al. 2014*). In contrast, observations during tropical storms
147 ($U_{10} \geq 18 \text{ m s}^{-1}$) and hurricanes ($U_{10} \geq 33 \text{ m s}^{-1}$) do not show the presence of stably-stratified
148 RLs (*D'Asaro et al. 2012, Jourdain et al. 2015*). From these previous studies, it remains unclear
149 whether 9.5 m s^{-1} represents the upper limit of U_{10} at which a RL can form, and if indeed this
150 value is an upper limit, why that should be the case. According to these previous studies based
151 on field measurements, understanding the formation and evolution of RLs, including the effect of
152 wind speed on their lifetime, is complicated by several factors:

153 • in addition to local rain, freshwater from nearby rain can be advected by the current into
154 ocean sensors;

155 • RLs spread and propagate laterally like density currents (*Soloviev et al. 2015*);

156 • RL creation and longevity depend on upper ocean turbulence, waves, and wind mixing.

157 These factors explain why RL observations are not always highly-correlated to their generating
158 rain events and why RL detection is not guaranteed from every rain event even if near-surface
159 salinity measurements are available, as noted by *You (1995)*. Observations (*Asher et al. 2014*)
160 and model results (*Drushka et al. 2016*) suggest that shallow, stable near-surface vertical salinity
161 gradients generated by rain form primarily when the rain rate, $R, \geq 5 \text{ mm h}^{-1}$. For tropical ocean
162 conditions, the buoyancy produced by $R = 5 \text{ mm h}^{-1}$ is equal and opposite to the buoyancy
163 destroyed by a surface cooling on the order of $Q_{\text{Net}} = 400 \text{ W m}^{-2}$ (demonstrated in **Appendix A**,
164 also see *Dorrestein 1979*). Additional turbulence may also be provided by wind, waves, or
165 subsurface shear. Thus, when $R < 5 \text{ mm h}^{-1}$, the freshwater from rain tends to be mixed into the
166 water column by a combination of surface cooling and turbulent mixing so that a stratified
167 surface fresh layer does not form. *Miller (1976)* also modeled RLs, noting that initializing light
168 rain rates with strong winds (45 mm accumulation over 15 h while $U_{10} = 10 \text{ m s}^{-1}$) resulted in the
169 formation of a mixed layer that was 38-m deep with no detectable SSS or SST change. This
170 showed that the rain was mixed downward and formed a homogeneous layer. When high rain
171 rates were modeled with low wind speeds (45 mm accumulation over 4 h while $U_{10} = 5 \text{ m s}^{-1}$), a
172 RL formed at 0.76 m depth and the greatest changes in SST and SSS were observed.

173 Our current understanding of RLs motivates the following questions:

- 174 a) What is the maximum U_{10} under which a RL or RL-DWL can form and persist?
- 175 b) Is this upper limit of U_{10} a function of R ?

176 c) How often do RLs and RL-DWL combinations occur throughout the suppressed, disturbed,
177 active, and westerly wind burst (WWB) periods of the MJO?

178 The ocean surface buoyancy flux and the turbulent kinetic energy (TKE) input to the
179 ocean provided by wind are both functions of MJO phase (e.g. *Zhang 2005, Moum et al. 2014*).
180 This should impact the formation and persistence of surface stratification throughout the MJO
181 lifecycle. The penetration depth of wind mixing into the ocean is determined by a balance
182 between stabilizing buoyancy forces and TKE production as given by Monin-Obukhov theory
183 (*Lombardo and Gregg 1989, Brainerd and Gregg 1995, 1997, Price et al. 1986*). This theory
184 suggests that a near-surface stable layer can persist during high wind speeds provided the
185 stabilizing buoyancy flux is large enough. If this hypothesis is true, then RL and RL-DWL
186 formation should be most likely in disturbed and active MJO periods when high rain rates occur,
187 even though surface wind speed may be great at times (e.g. *Zhang 2005, de Szoeke et al. 2014,*
188 *2017*). In the western Pacific warm pool, RL formation was observed during a WWB with
189 prolonged rain and $U_{10} = 9.5 \text{ m s}^{-1}$ (*Wijesekera et al. 1999*). This indicates that RL formation is
190 possible during WWBs despite strong winds. In contrast to RLs, DWLs have typically only been
191 observed during the suppressed phase of the MJO and when $U_{10} \leq 6-7 \text{ m s}^{-1}$ (*Webster et al. 1996,*
192 *Bellenger and Duval 2009, Matthews et al. 2014*). As will be shown in this study, the buoyancy
193 created by rain is typically an order of magnitude greater than that due to maximum net surface
194 heating. Therefore, it stands to reason that RLs should form and persist at higher U_{10} than DWLs,
195 and RLs should also occur in disturbed and active stages of the MJO, after the suppressed MJO
196 period that is characterized by frequent DWLs.

197 This study makes use of ship-based surface observations, including measurements of air-
198 sea fluxes, radar-observed rain, and in situ vertical profiles of ocean salinity and temperature.

199 These data are used to better understand how wind stress interacts with the buoyancy flux in the
200 formation and evolution of DWLs, RLs, and RL-DWLs observed throughout the MJO lifecycle.
201 The data used were collected in the central Indian Ocean throughout the two MJO cycles
202 observed during the 2011 Dynamics of the MJO (DYNAMO) experiment (*Johnson and*
203 *Ciesielski 2013, Yoneyama et al. 2013, Moum et al. 2014*). A method is developed for identifying
204 the presence of a near-surface ocean stable layer. This method is used to track ocean
205 stratification from the combined effects of diurnal warming and rain and to explore the
206 sensitivity of stable layer formation and persistence to U_{10} . Observations are compared to
207 estimates of stable layer depth and stable layer wind limits that were derived from Monin-
208 Obukhov similarity theory.

209 **2. Observations and Analysis Methods**

210 **a. Field program**

211 Here we examine 42 days of DYNAMO observations made from the research vessel
212 (R/V) *Roger Revelle* at 0°N and 80.5°E (*Johnson and Ciesielski 2013, Yoneyama et al. 2013,*
213 *Moum et al. 2014*). We examined times when precipitation radar, upper ocean, and surface data
214 were all available: from 5 Oct – 28 Oct and 12 Nov – 2 Dec 2011. These two time periods are
215 separated by a 15-day restaffing, refueling, and transit period.

216 Four time periods of the MJO were identified for this study region using the Real-time
217 Multivariate MJO (RMM) Index (**Table 1**, <http://monitor.cicsnc.org/mjo/curent/rmm/>). The
218 RMM Index describes MJO conditions by combining tropical atmospheric measurements of
219 outgoing longwave radiation (i.e. cloudiness) and zonal winds at 850 and 200 mb (*Wheeler and*
220 *Hendon 2004*). Numerous previous studies use the eight phases of the RMM Index to describe
221 MJO conditions (e.g. *Zhang 2005, Lau and Waliser 2005, Johnson and Ciesielski 2013,*

222 *Gottschalck 2013, Rowe and Houze 2015, Xu and Rutledge 2014, 2015*). Since phases 4, 5, 6,
223 and 7 of the RMM Index were not comprehensively observed during DYNAMO, the eight RMM
224 Index phases were organized into only four time periods of MJO conditions that were specific to
225 the central Indian Ocean location of this study (**Table 1**). The four time periods (suppressed,
226 disturbed, active, westerly wind burst / WWB), were mutually exclusive.

227 In the central Indian Ocean, the suppressed period is observed during RMM phases 5, 6,
228 7, and 8. Excluding the beginning of phase 5, these days typically have weak winds and
229 infrequent clouds and rain. DYNAMO days with upper ocean observations did not coincide with
230 phases 5-6, so suppressed MJO days in this study only spanned phases 7-8. In November 2011,
231 phase 7 only lasted three total days and observations were only collected on the last day;
232 however, observations were collected during all four days of phase 8 in this month. In October
233 2011, data was collected on all ten days of phases 7-8. The local onset of the disturbed MJO
234 (RMM phase 1) coincided with more frequent clouds and precipitation. Observations were
235 collected on all twelve days of phase 1 that occurred over both months. On active MJO days
236 (RMM phases 2, 3), rain and clouds persisted throughout a majority of the daytime hours
237 according to ship radar data. All ten days of these conditions were observed. According to the
238 definition by *Harrison and Vecchi (1997)*, the WWB time period occurred in this study region on
239 days when the RMM Index was 3-4 and when sustained $U_{10} > 7 \text{ m s}^{-1}$ for more than one day.
240 Observations were not collected during phase 4, but one and five days of WWB conditions in
241 phase 3 were observed in October and November, respectively. The 42 total observation days are
242 made up of 14, 12, 10, and 6 days of suppressed, disturbed, active, and WWB time periods
243 (**Table 1**).

244 **b. Surface meteorology and air-sea fluxes**

245 Near-surface meteorology (air temperature, specific humidity, and wind speed/direction
246 at nominally 10-m above the surface) and air-sea flux estimates are at
247 <ftp://dynamo.dms.uconn.edu/> linked by the Earth Observing Laboratory (EOL) field catalog:
248 http://data.eol.ucar.edu/master_list/?project=DYNAMO. Air-sea fluxes were computed using
249 the COARE 3.5 bulk aerodynamic algorithm (Fairall et al. 1996b, Fairall et al. 2003, Edson et
250 al. 2013, see complete description in de Szoeke et al. 2014). These data are available at 1- and
251 10-minute resolution. The 10-minute flux and surface data were utilized to match 10-minute
252 resolution precipitation radar data and interpolated ocean data. A 10-minute resolution time
253 series of R from the ship was acquired by resampling the 1-minute instantaneous R data from
254 ship gauges without performing any temporal smoothing. The net heat flux, Q_{Net} , was defined
255 negative downward into the ocean (heating the ocean) and positive upward out of the ocean
256 (cooling the ocean).

257 **c. Precipitation**

258 NASA TOGA C-band Doppler data from the R/V *Revelle* are also found on the EOL
259 field catalog (http://data.eol.ucar.edu/master_list/?project=DYNAMO). These were quality-
260 controlled to remove second trip echo and sea clutter and to correct for attenuation (details in Xu
261 and Rutledge 2014). Polar-coordinate data were gridded using RadX2Grid, provided by the
262 National Center for Atmospheric Research
263 (https://www.ral.ucar.edu/projects/titan/docs/radial_formats/radx.html), to a 0.5 km horizontal,
264 0.75 km vertical Cartesian grid within 25 km range of the ship. Coarser 2 km horizontal
265 resolution gridded data were also investigated out to the full range of the radar, 150 km, but are
266 not presented herein. Radar data were at 10-minute resolution. The radar's "cone of silence"
267 limited the first usable radar data to 2 km range. Radar reflectivity, Z_h , was partitioned into

268 convective and stratiform rain areas using the algorithm by *Yuter and Houze (1998)*. Then R was
269 estimated in each area with either a convective or stratiform equation for $R(Z_h)$, which were fit to
270 account for tropical oceanic rain variability by *Thompson et al. (2015)*. Separate convective and
271 stratiform $R(Z_h)$ equations help reduce error in R estimation compared to treating the entire Z_h
272 field with a single $R(Z_h)$ equation fit to all data (*Thompson et al. 2015*). More details about these
273 radar data procedures are in **Appendix B**.

274 Radar data were queried to identify times when precipitation existed upstream of the
275 research ship. The research ship was always directed westward into the eastward-flowing surface
276 current, which was typically 0.8 m s^{-1} . A rain sector area was defined to extend 9 km from the
277 ship in the upstream direction, between $235\text{-}300^\circ$, and to extend 4 km away from the ship in all
278 other directions (**Fig. 1**, 104 km^2 total sector area). Sector extensions of 9 and 15 km were tested,
279 which corresponded to advective time scales of about 3 h and 4.5 h from the upstream edge of
280 the sector to the ship. Upper ocean evolution related better to rain within the sector that extended
281 only 9 km upstream, so this extension distance was chosen for the rest of this study.

282 Values of R from the ship radar's rain sector and from the ship's gauge were combined to
283 form a 10-minute resolution time series of R_{MAX} , the maximum R sampled from either the ship
284 gauge or within the radar sector. Using this time series of R_{MAX} , 119 periods of rain were
285 identified over the course of 42 intensive observation days. In order to qualify as a new rain
286 event, rain was required to have not occurred for the previous 30 minutes. Rain event
287 classification did not involve a minimum duration threshold, so the shortest rain event was the
288 same resolution as the dataset, 10 minutes.

289 **d. Ocean T and S**

290 SST and bulk near-surface values of temperature, T, and salinity, S, were provided in the
291 flux dataset discussed above. SST was measured at roughly 0.05 m depth by a towed thermistor
292 contained within a brass body that was sealed inside a floating Tygon tube, i.e. inside a sea snake
293 (*Fairall et al. 1997*). Bulk T and S were measured by the ship's thermosalinograph (TSG) using
294 an intake at 5 m depth at the bow of the ship. The Chameleon profiler (*Moum et al. 1995*) was
295 deployed from the stern of the ship and provided vertical profiles of S and T at 7-minute
296 intervals with 1-m vertical resolution between 350 m depth and the sea surface depending on
297 waves and swell. These data were mixed by the ship's wake, so useful measurements began at 2-
298 3 m depth. Ten thermistors sampling T at least 20 times per minute were also tethered along a
299 chain at a distance of 5 m away from the starboard bow. The thermistors were unequally spaced
300 between 1.5 and 7.5 m along the chain and their vertical positions varied by approximately 0.5-
301 1.0 m depending on the speed of the ship, the surface current, and surface gravity waves. These
302 data were interpolated to a 1-m vertical grid. When the ship was headed into a steady mean
303 eastward surface current, the thermistor chain provided a record of T measurements undisturbed
304 by the ship's wake (*Moulin et al. 2017*). In comparison, Chameleon profiling from the stern as
305 the ship remained stationary and pointed into the steady eastward current. This approach yielded
306 vertical profiles of T and S that were disturbed by the ship's propulsion system over at least the
307 top 7 m depth (the draft of *Revelle* is 5 m). In order to assemble vertical profiles of T and S that
308 were most representative of open-ocean conditions, sea snake SST data and thermistor chain T
309 data were used above 5 m, thermistor chain and Chameleon T data were averaged at 5 m and 6
310 m, and Chameleon T data were used at 7 m and below. Chameleon profiles provided the
311 shallowest and most temporally continuous set of S measurements, which were used exclusively
312 for S vertical profiles in this study. These vertical profiles of ocean T and S were resampled to

313 the 10-minute interval of radar and flux datasets without performing any temporal smoothing, i.e.
 314 data points closest in time to the 10-minute interval were used.

315 **e. Ocean stability**

316 Vertical T and S gradients were used to calculate N^2 , the Brünt-Vaisala frequency. The
 317 value of N is a measure of static stability and relates to the natural frequency of internal gravity
 318 waves:

$$N^2 = \frac{g}{\sigma} \frac{d\sigma}{dz} \quad [1]$$

319 where σ is the sea water potential density and z is the vertical coordinate, oriented positive
 320 downward. The value of N^2 is positive for a statically-stable layer of water and negative for
 321 unstable conditions that are prone to convective overturning and vertical mixing. The linear
 322 approximation of the equation of state of seawater leads to an N^2 expression that can be scaled by
 323 the individual effects of S and T on σ :

$$N^2 \cong N_{S+T}^2 \cong N_T^2 + N_S^2 \quad [2]$$

$$N_T^2 = g\alpha \frac{dT}{dz} \quad [3]$$

$$N_S^2 = g\beta \frac{dS}{dz} \quad [4]$$

324 where α [$^{\circ}\text{C}^{-1}$] is the thermal expansion coefficient of seawater:

$$\alpha = \frac{-1}{\sigma} \frac{\partial\sigma}{\partial T} \quad [5]$$

325 and β [PSU^{-1}] is the salt contraction coefficient of seawater:

$$\beta = \frac{1}{\sigma} \frac{\partial\sigma}{\partial S} \quad [6]$$

326 Signs in [5] and [6] reflect that density increases as water becomes colder and saltier, such that
 327 [3] and [4] describe how the water column becomes more stable when a lighter fluid sits atop a

328 denser fluid. The α and β coefficients were calculated using the Gibbs-SeaWater (GSW)
329 Oceanographic Toolbox (*McDougall and Barker 2011*) for each time and depth pair of S and T
330 measurements during DYNAMO. Then, N_S^2 and N_T^2 were calculated between each vertical level
331 at each time interval using estimated α and β and the measured vertical S and T gradients. Fields
332 of N^2 were smoothed with a 3-m vertical running mean filter with 1-1-1 weighting. Vertical
333 profiles of N_{S+T}^2 calculated with [2] were nearly equivalent to vertical profiles of N^2 calculated
334 directly from the vertical density gradient in [1]. Therefore, N_{S+T}^2 from [2] is used throughout
335 this study and is abbreviated henceforth as N^2 . Estimates of N_S^2 were available starting at 2-3 m,
336 while estimates of N_T^2 were available from 0-350 m. Therefore, N^2 was determined solely by N_T^2
337 above 2 m depth.

338 **f. Ocean stable layer identification algorithm**

339 Depth ranges were considered well-mixed if $-4.5 \times 10^{-5} < N^2 < 4.5 \times 10^{-5} \text{ s}^{-2}$ over at least 3
340 consecutive meters vertically. Water was considered stable if $N^2 > 4.5 \times 10^{-5} \text{ s}^{-2}$ for at least 2
341 consecutive meters vertically. Using these definitions, an algorithm was devised to search for the
342 top of the shallowest stable level in the ocean column, h_S , at 10-minute intervals. The algorithm
343 also determined the base of the shallowest stable layer, h_B . Stable layers were required to be at
344 least 2-m in vertical thickness in this study because data with 1-m vertical resolution were used.
345 Therefore, the minimum stable layer thickness in this study was 2 m (i.e. $h_B - h_S \geq 2 \text{ m}$). The
346 minimum depth of h_S was 0 m. The top depth of the thermocline, h_{TC} , was defined as the first
347 level over which $N^2 > 1.75 \times 10^{-4} \text{ s}^{-2}$ for at least 3 consecutive meters. If the algorithm could not
348 identify a stable layer shallower than 45 m or within 10 m of h_{TC} , the ocean was considered to be
349 well-mixed from the surface to the thermocline and h_S was reassigned to h_{TC} . In this case, the
350 shallowest stable layer was the thermocline and $h_S = h_{TC}$. These thresholds and methodology

351 were manually tested until the algorithm yielded physically consistent results across all 42 days
352 of analysis. After these rules were applied, h_S , h_B , and h_{TC} were smoothed with a running 50-min
353 filter with 1-1-2-1-1 weighting.

354 The quantities $\overline{N_S^2}$ and $\overline{N_T^2}$ were determined by vertically-averaging the N_S^2 and N_T^2 fields
355 between 0-5 m and then smoothing the resulting time series with a running 30-min filter with 1-
356 2-1 weighting. RLs and DWLs were defined to begin when $\overline{N_S^2}$ and $\overline{N_T^2} > 1.5 \times 10^{-5} \text{ s}^{-2}$,
357 respectively, and $h_S \leq 5$ m. Not all DWLs or RLs were associated with the creation of a new
358 stable layer or with h_S shoaling because near-surface stratification with respect to the other state
359 variable (S or T) could have already existed. RL and DWL events were determined to end when
360 $\overline{N_S^2}$ and $\overline{N_T^2} < 1 \times 10^{-7} \text{ s}^{-2}$, respectively, or when $h_S > 5$ m, whichever event occurred first. To be
361 classified, RL and DWL events were required to last at least 3 consecutive observations
362 (spanning 30 total minutes) and be at least 1 h apart from stable layers of the same type.
363 Therefore, a RL could form in close succession to a DWL, but, in order to be classified as an
364 individual event, the RL must be at least 1 h away from the next or previously-identified RL.

365 Bow N_T^2 profiles extended to the surface, whereas stern N_S^2 profiles began at 2-3 m. The
366 bow N_T^2 profiles did not suggest that cold, fresh layers were deposited by rain shallower than 2
367 m. In other words, the N_T^2 data do not suggest that RLs were missing from N_S^2 profiles, although
368 it is possible the T profiles did not capture all stratification events. Even if RLs began earlier or
369 shallower than suggested by the S measurements from 2-3 m, the stable S gradients ought to mix
370 downward past the 2-3-m measurements throughout the lifetime or decay of the RL. Therefore,
371 our record of RLs is most likely not comprehensive, but our record should be representative of
372 the majority of RLs that occurred at this central Indian Ocean location during DYNAMO.

373 Our RL and DWL identification algorithm is demonstrated on a time period beginning at
374 00:00 UTC, 30 min prior to sunrise (**Fig. 2**). On this day, which was classified as “active” MJO
375 conditions, a DWL formed at 06:00 UTC (local noon) as Q_{Net} reached -300 W m^{-2} and U_{10}
376 decreased to below 4 m s^{-1} (**Fig. 2a, 2d**) The DWL was marked by strongly positive N_T^2 above 5
377 m depth and $h_S = 0 \text{ m}$ (**Fig. 2e**). Rain fell intermittently upstream of the ship during the DWL
378 between 07:00-10:00 UTC, mid-afternoon (**Fig. 2b**). Rain only occurred locally at the *Revelle*
379 between 09:30–10:00 UTC. Contemporaneously with the local rain accumulation, N_S^2 became
380 positive over the same depths as the DWL, making this a RL-DWL combination (**Fig. 2d, 2e,**
381 **2f**). Stratification of both S and T disappeared at 14:00 UTC (08:00 PM) as U_{10} increased rapidly
382 to $6\text{-}8 \text{ m s}^{-1}$ while $Q_{\text{Net}} \sim 100\text{-}200 \text{ W m}^{-2}$, indicating the ocean surface was cooling (**Fig. 2a, 2d,**
383 **2e, 2f**). Rain occurred upstream of the ship from 15:00-17:00 UTC (evening) while U_{10} reached
384 $6\text{-}8 \text{ m s}^{-1}$ (**Fig. 2a, 2b**). There was no RL observed locally as a result of this upstream rain event
385 (**Fig. 2d, 2e, 2f**). Instead, N_S^2 and N_T^2 indicated that the ocean was well-mixed between the
386 surface and a depth of 30 m.

387 Later that night at 17:00 UTC, 11:00 LST, the wind weakened ($U_{10} < 2 \text{ m s}^{-1}$) and a large
388 area of weak-to-moderate rain began upstream of the ship ($R_{\text{MAX}} = 7 \text{ mm h}^{-1}$, **Fig. 2a, 2b**).
389 Following this series of events, N_S^2 and N_{S+T}^2 became strongly positive near the ocean surface,
390 indicating the presence of a second RL (**Fig. 2d**). Within this nighttime RL, N_T^2 was negative due
391 to the combined cooling effects of rain, latent, sensible, and radiative fluxes (**Fig. 2e**). The
392 unstable N_T^2 within the RL due to surface cooling was not large enough magnitude to render the
393 entire layer unstable, since N_{S+T}^2 (i.e. N^2) remained mostly positive (**Fig. 2f**). The nighttime RL
394 lingered above 5 m depth for over 6 hours after upstream rain ended (**Fig. 2b**). The daytime RL
395 persisted 4 hours after upstream rain ended, 5 hours after local rain ended. Both RLs were

396 coincident with 2- and 3-m depth freshening trends and fresher 2-m S compared to 3-m S (**Fig.**
397 **2c**), leading to stable vertical gradients of S and therefore positive N_S^2 (**Fig. 2d**). During the
398 DWL, RL, and RL-DWL events, $h_S \leq 5$ m and the stable layer thickness, $h_B - h_S$, was roughly 2 m
399 (**Fig. 2d, 2e, 2f**). This daily analysis was used to test the stable layer identification algorithm on
400 all 42 DYNAMO observation days.

401 **3. Results**

402 This section examines the frequency of occurrence of RLs, DWLs, and RL-DWLs
403 observed throughout two MJO cycles during DYNAMO and the conditions in which these stable
404 layers existed.

405 **a. Stable layer occurrence and depth**

406 From our DYNAMO record, rain and surface warming both played significant roles in
407 creating stable near-surface ocean conditions in which $h_S \leq 5$ m (**Fig. 3, Table 2**). Throughout 42
408 observation days, stratification existed above 5 m over the course of 44 events due to the
409 presence of one or more stable layers: 14 DWL-only events, 14 RL-only events, and 16 events in
410 which RLs and DWLs combined one or more times. We sampled 30 DWLs (299 observation
411 hours, 30% of the data record) and 32 RLs (165 hours, 16% of the data record). RL-DWL
412 combinations were almost two times more likely to be RLs contained within preexisting DWLs
413 than vice versa. For example, 10 DWLs contained one or more RLs and only 6 RLs contained
414 DWLs; 12 RLs formed on top of preexisting DWLs but only 7 DWLs formed on top of
415 preexisting RLs. The total number of continuous stratification events in which RLs and DWLs
416 combined was only 16 even though 18 individual RL-DWL events were observed. This is
417 because one DWL contained 2 RLs and another DWL formed in a preexisting RL that also later
418 contained a new RL. RL-DWLs occupied 89 hr, or 9%, of the DYNAMO data record. RLs

419 without DWL influence spanned only 8% of the dataset, while DWLs without RL influence
420 spanned over twice as much (21%) of the dataset. Collectively over the course of two MJOs,
421 daytime warming and rain caused stable layers to exist in the upper 5 m of the ocean during 38%
422 of the dataset, and in the upper 10 m during 57% of the dataset (**Fig. 3, Fig. 4**).

423 When RLs and DWLs were not present, water was mixed between the surface and the
424 thermocline, meaning the shallowest ocean stable layer was the thermocline and $h_S = h_{TC}$ (**Fig.**
425 **3**). This situation occurred during 13% of the dataset. When RLs and DWLs decayed, these
426 stable layers mixed downward to about 40 m depth in October 2011 (days 5-13, 21-27). In
427 November 2011, a month during which a stable barrier layer existed between 10-30 m, RLs and
428 DWLs only mixed downward to about 10 m depth (**Fig. 3**, days 14-24). During the first
429 November WWB pulse on 24-26 November, this barrier layer eroded and the thermocline
430 rapidly deepened from 57 m to 90 m (**Fig. 3, Fig. 4c**, also discussed by *Moum et al. 2014* and
431 *Chi et al. 2014*). Abrupt shifts in vertical T and S stability structure were noted on 18 and 24
432 October and 12, 14, 15, and 18 November, which appear to be the result of advection (discussed
433 further in Sec. 3b and by *Chi et al. 2014*).

434 RLs, DWLs, and RL-DWL combination stable layers were most frequently observed to
435 be between 2-8 m thick, with a mean thickness of 6 m and median thickness of 4 m (**Fig. 3** and
436 **Fig. 4b**). These thickness observations are only slightly greater than the 2-4 m thickness
437 estimates from previous modelling studies (*Miller 1976, Price 1979, Price et al. 1986,*
438 *Lombardo and Gregg 1989, and Lukas and Lindstrom 1991, Drushka et al. 2016*).

439 While this dataset's mean stable layer depth, $\overline{h_S}$, of 20 m agrees with the 18-m mean
440 mixed layer depth estimate based on Argo profiles for this location in October-November from
441 *de Boyer Montegut et al. (2004)* and also roughly with the 36 m mean depth from *Holte et al.*

442 (2017), the high-resolution values of h_S from DYNAMO were only within ± 5 m of the mean
443 value, $\overline{h_S}$, during 9% of the dataset (**Fig. 3, Fig. 4**). In the other 91% of the dataset, the
444 penetration depth of wind mixing was either over- or under-estimated by $\overline{h_S}$ by at least 20 m,
445 which led to errors of 100% or greater. The standard deviation of h_S was 25 m, greater than the
446 20-m mean value, $\overline{h_S}$. Thus, $\overline{h_S}$ and the mean mixed layer depths from Argo are not
447 representative of the daily and sub-daily upper ocean stabilization events observed during this
448 experiment (**Fig. 3, Fig. 4**). For instance, rain and diurnal heating stabilized the upper 5 m of the
449 ocean on 37 out of 42 observation days, while waters were well-mixed between the surface and
450 40-60+ m depth on 20 out of 42 days. Instances of $h_S = 20$ m (i.e. $h_S = \overline{h_S}$) were brief, occurring
451 only as stable layers were forming, deepening, or decaying.

452 **b. Wind limits of stable layers**

453 The 99th percentile value of U_{10} observed in the presence of stable layers was 9.8 m s^{-1}
454 for RLs, 7.6 m s^{-1} for DWLs, and 5.5 m s^{-1} for RL-DWLs. These values are considered to be the
455 wind limits on each type of stable layer. Very few instances occurred in which RLs were present
456 and $U_{10} > 10 \text{ m s}^{-1}$ (9 data points) or in which DWLs were present and $U_{10} > 7 \text{ m s}^{-1}$ (27 data
457 points total, **Fig. 5**). The overall highest value of U_{10} observed during a RL was 11.3 m s^{-1} ,
458 compared to 9.2 m s^{-1} in a DWL and 6.3 m s^{-1} in RL-DWLs (**Fig. 5**). Numerous previous studies
459 have also found that DWLs are limited to times when $U_{10} \leq 7 \text{ m s}^{-1}$ (e.g. *Fairall et al. 1996b*,
460 *Webster et al. 1996*). Results herein are also consistent with a RL observed in the equatorial
461 western Pacific Ocean during which $U_{10} = 9.5 \text{ m s}^{-1}$ (*Wijesekera et al. 1999*). In the absence of
462 RLs or DWLs, i.e. when the upper ocean was well-mixed, U_{10} ranged from 0 to 17.6 m s^{-1} and
463 the 99th percentile value of U_{10} was 13.9 m s^{-1} (**Fig. 5**).

464 **c. Occurrence of stable layers throughout the MJO lifecycle**

465 Of the 44 continuous stable layer events observed, a similar number of events occurred in
466 each of the suppressed, disturbed, and active periods of the MJO (13, 17, and 12 events,
467 respectively) but only 2 stable layer events occurred in the WWB period (**Table 2, Fig. 6**). The
468 occurrence of RLs and DWLs over the MJO lifecycle mirrors the well-documented evolution of
469 U_{10} , R , and Q_{Net} throughout the MJO (**Table 1, Fig. 6**, e.g. *Zhang 2005, Rickenbach and*
470 *Rutledge 1998, Johnson et al. 1999, Barnes and Houze 2013, Xu and Rutledge 2015*). For
471 example, little rain occurred during the suppressed MJO period (**Fig. 6, Table 1**). In these
472 conditions, only two RL-DWL events and no RL-only events were observed (**Fig. 6, Table 2**).
473 During the disturbed and active MJO periods, $U_{10} < 8 \text{ m s}^{-1}$ and rain was frequent, intense, and
474 long-lasting (**Fig. 6, Table 1**, e.g. *Xu and Rutledge 2014*). Within these disturbed and active
475 MJO periods, RLs and RL-DWLs occurred once or more per day (**Fig. 6, Table 2**). During
476 WWBs, when rain was frequent and long-lived but U_{10} was very strong, RLs were rarely
477 observed (**Fig. 6, Table 1, Table 2**). Within WWBs, mean $U_{10} = 9.1 \text{ m s}^{-1}$ and max $U_{10} = 17.6 \text{ m}$
478 s^{-1} , **Fig. 6, Table 1**). In contrast, DYNAMO observation days outside of WWBs exhibited much
479 weaker winds, with mean $U_{10} = 3.6 \text{ m s}^{-1}$ and max $U_{10} = 11.3 \text{ m s}^{-1}$ (**Fig. 6, Table 1**).

480 Similar to results from previous studies, DWLs consistently formed on days when $Q_{\text{Net}} <$
481 -600 W m^{-2} (heating the ocean), and $U_{10} \leq 7 \text{ m s}^{-1}$ (**Fig. 5, Fig. 6, Fairall et al. 1996a, Webster**
482 *et al. 1996, Matthews et al. 2014, Asher et al. 2015, Moulin et al. 2017*). DWLs were not
483 observed when one or both of these conditions were not met, such as on 13 October in the
484 suppressed period, on 19, 24, and 25 October, and 22 November during disturbed and active
485 periods, and during all WWB days (**Fig. 6**). As a result, DWLs of some form occurred on 92% of
486 observed suppressed period days (all but one day), 83% of disturbed MJO days, and 70% of
487 active MJO periods, but DWLs did not occur at all during WWBs (**Table 2, Fig. 3, Fig. 6**).

488 Of the 17 DWLs observed outside of the suppressed MJO period, 14 (82%) were actually
489 RL-DWL combinations at one point. RL-DWLs combinations occurred in 8/10 observed DWLs
490 during disturbed MJO periods, and in 6/7 DWLs during active MJO periods (**Fig. 6, Table 2**).
491 DWLs and RLs were only observed to overlap once at the beginning of each DYNAMO
492 suppressed phase. No RL-DWL combinations (or DWLS) were observed during WWBs (**Fig. 6,**
493 **Table 2**). Overall, RL-DWL combinations only occurred during 9% of the DYNAMO period,
494 but totaled to a substantial portion of the total 44 stable layers observed, 16 events or 36%.

495 **d. Diurnal variability and duration of stable layers**

496 In contrast to DWLs, RLs were observed at all hours of the day and night (**Fig. 7b, 7e**).
497 Out of 32 RLs observed, 18 (56%) existed at some point during overnight hours between sunset
498 (00:30 UTC) and sunrise (12:30 UTC); 20 RLs (62%) existed at some point during the daytime.
499 During DYNAMO, rain occurred at all hours of the day but its intensity peaked in late-afternoon
500 and also just before dawn (**Fig. 7a**), as typically found over tropical oceans (e.g. *Yang and Slingo*
501 *et al. 2001, Sakaeda et al. 2018*). In alignment with the diurnal cycle of R , RL likelihood also
502 peaked slightly in the afternoon, reaching 29% at 8 UTC (2 PM LST, **Fig. 7b**). RL likelihood
503 was at least 7% at all other hours of the day (**Fig. 7b**). Both DWLs and RL-DWLs existed
504 primarily during the daytime (2-22 UTC), with a peak in probability of occurrence between 5-10
505 UTC (11 AM-4 PM LST, **Fig. 7e, 7h**). There was a high (66-68%) likelihood of a DWL being
506 present between 6-8 UTC (local noon to 3 PM). For RL-DWLs, the peak likelihood occurred at a
507 similar time, from 7-9 UTC (1-4 PM LST), but the peak was not as prominent (19-23%).

508 Stable layers of all types were less likely to occur at night (**Fig. 7b, 7e, 7h, 7k**). The
509 likelihood of continuous stable layer events, which could contain one or more RLs and/or DWLs,
510 was as low as 10% overnight and as great as 77% at 7 UTC (1 PM, **Fig. 7k**). At night, $Q_{\text{Net}} > 0$,

511 i.e. surface cooling, and hourly-mean U_{10} was slightly greater than in the daytime (**Fig. 7a**). Both
512 of these factors promote convection in the oceanic boundary layer, and could have contributed to
513 the reduced occurrence of stable layers at night.

514 RLs formed at all hours of the day, but DWLs and RL-DWLs began preferentially during
515 the daytime (**Fig. 7e, 7f, 7i**). DWLs exhibited a strong peak in hour of formation at 3 UTC, 3 h
516 after sunrise (**Fig. 7f**). As a result, the peak in formation of all continuous stable layer events was
517 also strongly peaked at 3 UTC (**Fig. 7i**). RLs and RL-DWLs were only slightly more likely to
518 form at 3 and 4 UTC compared to other hours (**Fig. 7c, 7i**).

519 The average hour in which existing DWLs became absent from the upper 5 m was 14:00
520 UTC (1.5 h after sunset). Out of 32 total RLs observed, 11 (34%) formed at night. Four night-
521 time RLs lasted into the next daytime cycle and seven daytime RLs lasted at least 3 h past sunset.
522 DWLs persisted several hours after sunset during the November suppressed period when a
523 barrier layer existed between 10-20 m depth (**Fig. 3, Fig. 7e**). During these very stable upper
524 ocean conditions, DWLs also often formed shortly after dawn.

525 From the Eulerian perspective of this stationary research ship experiment, RLs were
526 observed locally over durations ≤ 14 h, RL-DWLs were observed for shorter durations (≤ 11 h),
527 and DWLs were observed for the longest durations (≤ 21 h, **Fig. 7d, 7j, 7g**). The 21-h DWL
528 event occurred on 15 Nov 2011 (**Fig. 3**), having formed at the surface at 2 UTC on top of a salt-
529 and temperature-stratified barrier layer that had risen to within 5-10 m of the surface. By mid-
530 afternoon, the base of the DWL merged with the underlying barrier layer and the combined near-
531 surface stable layer remained within 5 m of the ocean surface until 23 UTC. Using satellite
532 (*Stuart-Menteth et al. 2002, Clayson and Bogdanoff 2013*) and reanalysis (*Bellenger and Duvel*
533 *2009*) datasets, DWLs have been found to last over 5 days and cover expansive regions of the

534 ocean (1000 km or more wide). From the Eulerian point of view of the ship, the mean duration of
535 DWLs (10 h) was double the mean duration of RLs and RL-DWLs (5 h). The Lagrangian, or
536 water-following, lifetime of stable layers could be longer than suggested by the measurements
537 obtained during DYNAMO. The average duration of all continuous stable layer events was 8 h
538 (**Fig. 7m**). Minimum RL, DWL, and RL-DWL durations were all 30 minutes because of the 10-
539 minute resolution of this dataset. Given the average speed of the surface current during each RL,
540 the equivalent mean and maximum length scales of RLs were 9.2 and 33.2 km. However this
541 length-scale estimate is approximate because it does not account for lateral mixing of the RL or
542 the spatial and temporal heterogeneity of precipitating systems (*Wijesekera et al. 1999, Soloviev*
543 *and Lukas 2006, Houze et al. 2015*).

544 The longest-lasting RL was one that formed in a DWL (14 h). The mean durations of RLs
545 with and without DWL influence were not significantly different. Similarly, DWLs with and
546 without RL influence were not necessarily longer or shorter; both DWL varieties had a mean
547 duration of 10 h. Ignoring the relative timing of T and S stratification, the overall mean duration
548 of RL-DWL combinations was 5 h (**Fig. 7j**). RLs that formed on DWLs and DWLs that formed
549 on RLs could be phenomenologically distinct, but a larger dataset of these features is required to
550 precisely determine their differences. Thus, these two cases have been combined into a single
551 category, RL-DWLs, for this study.

552 **4. Stable Layer Estimates**

553 This section seeks a better understanding of the observed depth (**Fig. 3, Fig. 6**) and wind
554 limits (**Fig. 5**) of stable layers by examining estimates of each quantity:

555 (1) the upper ocean stable layer depth, \hat{h}_S ; and

556 (2) the highest values of U_{10} at which stable layers persist and form, \hat{U}_S .

557 **a. Stable layer depth: \hat{h}_S**

558 To clarify the relationship between h_S and U_{10} , we consider B , the surface buoyancy flux
559 into the ocean produced by the combined effects of rain and heating (**Fig. 8, Appendix A, Fig.**
560 **A1, Dorrestein 1979**), and u_{W*}^3 , the cubed friction velocity in the water, which we consider to
561 represent the rate of turbulent kinetic energy (TKE) input to the ocean surface by the wind; u_{W*}^3
562 [$\text{m}^3 \text{s}^{-3}$] is opposed by B [$\text{m}^2 \text{s}^{-3}$]. The value of B is a function of surface water properties, Q_{Net} ,
563 and R . For reference from **Appendix A**:

564 (1) $R = 10 \text{ mm h}^{-1}$, a typical tropical oceanic rain rate (*Thompson et al. 2015*), produces the
565 same buoyancy as $Q_{\text{Net}} = -850 \text{ W m}^{-2}$, the median daily max value of surface heating during
566 DYNAMO. According to this dataset, $\text{max } R = 188 \text{ mm h}^{-1}$ and 30% of R observations
567 exceeded 10 mm h^{-1} , which was also shown by *Thompson et al. (2015)* for two long-term
568 IndoPacific warm pool datasets of R . During DYNAMO, $Q_{\text{Net}} < -850 \text{ W m}^{-2}$ during only 1%
569 of observations ($\text{min } Q_{\text{Net}} = -1035 \text{ W m}^{-2}$). Therefore, rain can produce B that is more than
570 an order of magnitude greater than is typically produced by surface heating (**Fig. 8**).

571 (2) The buoyancy produced by $R = 5 \text{ mm h}^{-1}$ is equal and opposite to the buoyancy destroyed by
572 a surface cooling on the order of $Q_{\text{Net}} = 400 \text{ W m}^{-2}$, which is the maximum nighttime Q_{Net}
573 outside of WWB periods and maximum observed latent heat flux, Q_{Lat} . Since $R = 5 \text{ mm h}^{-1}$ is
574 a relatively weak rain rate and $Q_{\text{Net}} = 400 \text{ W m}^{-2}$ is a very high cooling rate, buoyancy
575 produced by rain typically stabilizes negative buoyancy produced by surface cooling.

576 (3) Buoyancy produced by rain freshening is 15 times greater than negative buoyancy produced
577 by rain cooling, meaning the cooling effect of rain on B can be ignored. B produced by rain is
578 always positive, which can lead to stratification of the upper ocean.

579 From a 1-D perspective and neglecting shear- and wave-driven turbulence, Monin-
 580 Obuhkov scaling suggests that B will be mixed by wind stress to an estimated depth of \hat{h}_S given
 581 by:

$$\hat{h}_S = \frac{u_{W*}^3}{\kappa B} \quad [7]$$

582 where $\kappa = 0.40$, the von Kármán constant, or

$$\hat{h}_S = C \frac{U_{10}^3}{B} \quad [8]$$

583 where the constant C includes the densities of seawater and air, ρ_W and ρ_{air} , and a drag
 584 coefficient, $C_D \sim 0.8-1 \times 10^{-3}$ (Edson et al. 2013):

$$C = \frac{1}{\kappa} \left(\frac{C_D \rho_{air}}{\rho_W} \right)^{3/2} \cong 5.42 \times 10^{-9} \quad [9]$$

585 [8] and [9] arise from the fact that the flux of momentum is continuous across the sea surface
 586 such that $\tau = \rho_W u_{W*}^2 = \rho_{air} u_{air*}^2$, where the τ in the air is approximated by $C_D \rho_{air} U_{10}^2$.

587 According to observations, if surface water is less dense than underlying water, $h_S \sim 0$ m
 588 and h_S marks the top of a stable layer that is in contact with the surface (**Fig. 2, Fig. 3**). In [7] and
 589 [8], $\hat{h}_S \sim 0$ for very large B and weak values of u_{W*}^3 or U_{10} , respectively. Equations [7] and [8]
 590 result from the assumption that the stable layer depth, h_S , responds to changing production and
 591 consumption of TKE. This approach is in contrast to a Richardson number constraint, which is
 592 applied with mixed layer models or simple layer-averaged slab models (Fairall et al. 1996a).

593 By isolating DYNAMO data for periods when $B > 0$, close agreement was found between
 594 \hat{h}_S and h_S (**Fig. 9**, in which h_S was temporally-averaged by a 1-h moving mean filter and \hat{h}_S was
 595 temporally-averaged by a 2-h moving mean filter). Of 44 total observed stable layers, 36 were
 596 successfully predicted to exist above 5 m depth by \hat{h}_S within the same time span that they
 597 occurred according to h_S (**Fig. 9**). This equates to an 88% success rate in terms of stable layer

598 prediction. All DWLs, all RL-DWLs, and all but 8 short-lived RLs were predicted by \hat{h}_S . During
599 times when \hat{h}_S mirrored h_S , we assume that the buoyancy and wind-mixing forces described in
600 [7, 8] were the dominant factors controlling the depth of upper ocean stratification, h_S . When $B <$
601 0, the ocean should mix vertically due to convective overturning by surface cooling or extreme
602 salinification. However, when $B < 0$, \hat{h}_S also becomes negative, the latter of which is non-
603 physical and is therefore not shown in **Fig. 9**. The estimated stable layer depth \hat{h}_S was able to
604 account for observed near-surface stratification better than the observed mean value, $\overline{h}_S = 20$ m,
605 or the monthly mean mixed layer depths, h_{M1} and h_{M2} , determined by two previous studies for
606 this location in October and November (**Fig. 9**, *de Boyer Montegut et al. 2004*: 17 and 19 m;
607 *Holte et al. 2017*: 34 and 37 m, respectively). The oscillation of h_S between its two extrema,
608 near-surface stratification or deep mixing, was not random, i.e. h_S did not randomly vary about
609 \overline{h}_S . Rather, the h_S oscillations systematically coincided with the occurrence of either buoyancy
610 production by rain and solar heating or buoyancy destruction by wind (**Fig. 6**, **Fig. 8**, **Fig. 9**).

611 Several 1-2 h temporal differences existed between estimated \hat{h}_S and observed h_S (**Fig. 9**).
612 These temporal differences appear reasonable given that h_S is an observation of a present state,
613 whereas \hat{h}_S is a prediction of a future equilibrated state given the present values of B and U_{10} .
614 Moreover, temporal and spatial averaging were performed in the estimation of both \hat{h}_S and h_S
615 time series, and S measurements were not collected above 2-3 m. For instance, the 1-2 h
616 temporal differences between \hat{h}_S and h_S appear understandable because RLs initially form within
617 the top several centimeters of the ocean (*Drushka et al. 2016*), they often propagate laterally
618 (*Soloviev et al. 2015*), and a finite amount of time is required for freshwater to be mixed and
619 diffused downward past the 2-3 m salinity measurements used in this study (*Asher et al. 2014*).

620 All of these aforementioned issues and processes could have contributed to the frequently-
621 observed 1-2 h timing offset between h_S and \hat{h}_S .

622 Aside from these slight timing differences, three additional differences were evident
623 between \hat{h}_S and h_S (**Fig. 9**):

- 624 (1) False Negatives: eight RLs were observed but not predicted, all of which occurred after
625 sunset on 10/17, 10/19, 10/22 (the second RL in **Fig. 2**), 10/27, 11/18, 11/19 11/20, and
626 11/22. These RLs were 1.5-4 h in duration. Local rain occurred during only two of the
627 missed RLs, whereas upstream rain was observed within 3 h of all eight events. These RLs
628 may have resulted from advection of near-surface freshwater. This could have led to their
629 under-prediction by \hat{h}_S , which relies on current conditions to predict stable layer existence.
630 One of the missed RLs formed inside a DWL that was correctly predicted, and that was
631 already in contact with the barrier layer (11/19).
- 632 (2) False Positives: three RLs were predicted but not observed. These occurred during WWBs
633 when contemporaneous *Revelle* measurements showed that sub-surface turbulence was
634 higher than would be expected from wind alone, having been enhanced by shear across a 50-
635 100 m depth Wyrтки Jet (*Moum et al. 2014*).
- 636 (3) Under-Predicted Duration: several DWLs, RLs, and RL-DWLs were observed to last longer
637 than predicted. DWLs and RLs can harbor stability near the surface well after B ceases to be
638 positive, particularly if U_{10} is weak, according to model simulations by *Drushka et al. (2016)*.
639 For instance, several DWLs lasted 3 h after sunset and the maximum observed duration of
640 DWLs and RLs was 21 and 14 h, respectively (**Fig. 7**), i.e. longer than the length of daytime
641 (12 h in this study) or the duration of individual rain events. Some of the stable layers with
642 underestimated duration occurred when the surface stable layers merged with the underlying

643 barrier layer (**Fig. 4**), meaning that the barrier layer could have influenced the lifecycle of
 644 certain stable layers. Under-predicted stable layer duration could also result from under-
 645 estimates of surface freshwater advection. The value of B was calculated with R_{MAX} , the
 646 maximum R observed from either the ship's gauges or the ship's radar within a sector
 647 spanning 9 km in the upstream direction (roughly a 3-h advective time scale) and 4 km in all
 648 other directions (**Sec. 2, Fig. 1**). We acknowledge the limitation of this method to account for
 649 the spatial heterogeneity of B due to rain.

650 **b. Stable layer wind limit: \hat{U}_S**

651 [8] and [9] can be rearranged to describe the wind limit of stable layers, \hat{U}_S , defined as
 652 the highest value of U_{10} in which stratification should exist at the depth h_S for a given value of B :

$$\hat{U}_S = \left(\frac{\hat{h}_S B}{C} \right)^{1/3} \cong 569 (\hat{h}_S B)^{1/3} \quad [10]$$

653 If $B > 0$ and $U_{10} \leq \hat{U}_S$, then conditions should be favorable for the formation and persistence of
 654 stable layers at or above the depth h_S . On the other hand, if $B > 0$ but $U_{10} > \hat{U}_S$, surface-forced
 655 mixing should outweigh buoyancy suppression and neither DWLs nor RLs should form at or
 656 above the depth defined by h_S . In other words, wind mixing will homogenize T and S in a layer
 657 extending from the surface downward to the barrier layer or the thermocline (**Fig. 3, Fig. 9**).

658 Solutions for [7, 8, 10], appear in **Fig. 10** for $h_S = 1, 2, \text{ and } 5$ m: u_{W*}^3 and B are related
 659 linearly (**Fig. 10a**), whereas \hat{U}_S is proportional to $B^{1/3}$ (**Fig. 10b**). In these figures, lines of
 660 constant h_S show that stable layers should form at these depths for a given B and u_{W*}^3 (**Fig. 10a**)
 661 and therefore U_{10} (**Fig. 10b**). Alternatively, the lines of constant h_S also indicate the highest
 662 values of wind mixing that can take place while stable layers either form or persist for a given B .
 663 From [10], the stable layer wind limit, \hat{U}_S , is equal to 8.6 m s^{-1} for $R = 50 \text{ mm h}^{-1}$ and $h_S = 1$ m,

664 which means that $R = 50 \text{ mm h}^{-1}$ should maintain a RL with stable dS/dz gradients as shallow as
 665 1-m depth so long as $U_{10} \leq 8.6 \text{ m s}^{-1}$. For the same R value and $h_S = 5 \text{ m}$, the wind limit of RLs
 666 increases to $\hat{U}_S = 13.6 \text{ m s}^{-1}$, which is only slightly higher than the greatest value of U_{10} observed
 667 in a RL: 11.3 m s^{-1} (**Fig. 5**). Values of \hat{U}_S range between $8.0\text{-}13.6 \text{ m s}^{-1}$ for R between $10\text{-}50 \text{ mm}$
 668 h^{-1} , while $\hat{U}_S = 8.4 \text{ m s}^{-1}$ for the maximum observed surface heating: $Q_{\text{Net}} = -1035 \text{ W m}^{-2}$ [10].
 669 This estimated wind limit on DWLs is close to the observed wind limit, $U_{10} = 7.6 \text{ m s}^{-1}$ (the 99th
 670 percentile value of U_{10} when DWLs were present, **Fig. 5**). An additional interpretation of these
 671 calculations is that a DWL may persist above 5 m when $U_{10} = 8.4 \text{ m s}^{-1}$ if Q_{Net} is maximized ($-$
 672 1035 W m^{-2}), while a RL may persist at the same depth and during the same wind speed even if
 673 R is only moderate (12 mm h^{-1}). Since instances of $R > 12 \text{ mm h}^{-1}$ are frequent, [8] and [10] can
 674 explain observations of RLs persisting at higher U_{10} than DWLs (**Fig. 5, Fig. 10**).

675 For all instances in which stable layers were present, 46% of DWL-only, 70% of RL-
 676 only, 70% of RL-DWL, and 66% of all stable layer instances occurred when $U_{10} < \hat{U}_S$ and $B > 0$
 677 $\text{m}^2 \text{ s}^{-3}$, when \hat{U}_S was evaluated with [10] assuming $h_S = 5 \text{ m}$. These percentages represent the
 678 success rates at which near-surface stable layer occurrence can be estimated by determining
 679 times when $U_{10} < \hat{U}_S$ and $B > 0 \text{ m}^2 \text{ s}^{-3}$.

680 The \hat{h}_S and \hat{U}_S methods predicted 36 out of 44 total stable layers to occur within the same
 681 time span that they were observed, leading to an overall success rate of 88% (**Fig. 9**). The
 682 remaining eight missed stable layers were RLs of relatively short duration, between 1.5-4 h, that
 683 occurred within 6 h of other observed (and successfully predicted) stable layers (**Fig. 9**). In other
 684 words, all observed DWLs, all observed RL-DWLs, and 75% of observed RLs were successfully
 685 predicted to occur within observed stable layer time spans.

686 The occurrence of $U_{10} < \hat{U}_S$ and $B > 0 \text{ m}^2 \text{ s}^{-3}$ was much more likely prior to the WWB
687 (**Fig. 5, Fig. 8, Fig. 9**). Values of U_{10} were rarely low enough to support stable layers during
688 WWBs, despite high B during this period (**Fig. 8, Fig. 9**). For example, only three RLs and no
689 DWLs were observed in WWBs. In suppressed, disturbed, and active MJO periods, conditions in
690 which $U_{10} < \hat{U}_S$ and $B > 0 \text{ m}^2 \text{ s}^{-3}$ occurred at least once per day (**Fig. 5, Fig. 9**). Stable layers
691 were frequently observed and predicted to occur during these periods (**Fig. 9**).

692 Both U_{10} and R were necessary for determining the likelihood of RL formation (**Fig. 11**),
693 while Q_{Net} alone could serve as a useful predictor for DWL occurrence (**Fig. 5, Fig. 11**). For
694 example, DWLs were only present during 15% of the time when $Q_{\text{Net}} > 0 \text{ W m}^{-2}$, and never
695 formed in these conditions, whereas DWLs were present 99% of the time when $Q_{\text{Net}} < -600 \text{ W}$
696 m^{-2} (**Fig. 11a**). The value of $Q_{\text{Net}} < -500 \text{ W m}^{-2}$ during every observed DWL (**Fig. 11a, Fig. 6**).
697 Thus, to a certain extent, the magnitude of Q_{Net} was a useful predictor of DWL occurrence even
698 without consideration of U_{10} (**Fig. 11b**). In contrast, many instances of $R = 0 \text{ mm h}^{-1}$ occurred
699 leading up to RL formation and when a RL was present. The probability distribution functions of
700 R were also not statistically different between times with or without the presence of a RL (**Fig.**
701 **11b**). In other words, RLs were not statistically more likely to occur at any R range except when
702 $R > 100 \text{ mm h}^{-1}$, and these high rain rates represent a small fraction of the total R distribution.
703 Therefore, the \hat{h}_S - and \hat{U}_S -based estimate of stable layer occurrence, which incorporates both U_{10}
704 and B (i.e. R), was more successful in determining the likelihood of RL formation compared to
705 predicting the existence of a RL using R alone (**Fig. 11d**).

706 **5. Discussion**

707 The presence of near-surface stable layers is important for coupled climate processes
708 because they limit the vertical extent of wind-driven ocean mixing and the distribution of

709 atmospheric forcing into the ocean (e.g. *Price et al. 1986, Fairall 1996a*). When either DWLs,
710 RLs, or their combinations are present, turbulent mixing must first supply enough kinetic energy
711 to homogenize the near-surface stable layers before mixing can extend deeper into the ocean
712 column. While formation of a DWL is limited to daytime since it requires solar warming, a RL
713 can form at any time. Furthermore, a RL may form within an existing DWL, and a DWL may
714 form within an existing RL (**Fig. 2, Fig. 6**). These two cases are considered together as RL-DWL
715 combinations in this study, though they could be phenomenologically distinct.

716 Based on the stable layer observations and estimates presented in **Sec. 3** and **Sec. 4**, we
717 hypothesize that the top depth of RLs and DWLs, h_S , can be reasonably predicted as \hat{h}_S in terms
718 of U_{10} and B and that the upper limit of U_{10} at which RLs and DWLs can form and persist, U_S ,
719 can be estimated in terms of B . This suggests that reasonable estimates of \hat{h}_S might be produced
720 from datasets of U_{10} and B over tropical oceans in which neither advection nor current shear are
721 dominant forces in the budgets of ocean buoyancy or momentum (**Fig. 9**). Measurements of U_{10}
722 and B are collected by moorings, ships, autonomous vehicles, and satellites. Estimates of U_{10} and
723 B are also available from several global products based on observations, such as reanalysis,
724 TropFlux (*Praveen Kumar et al., 2012*), and SeaFlux (*Curry et al., 2004*). Therefore, without the
725 use of subsurface ocean measurements, the \hat{h}_S and \hat{U}_S estimates could help determine when and
726 where the vertical extent of ocean mixing is limited to 0-5 m depth.

727 Furthermore, we hypothesize that the occurrence of RLs and DWLs throughout the MJO
728 is regulated by intraseasonal variations in U_{10} , Q_{Net} , and R as well as the local balance between B
729 and U_{10} (**Table 2, Fig. 6, Fig. 9**). Throughout the two MJO cycles observed during DYNAMO,
730 RLs withstood $U_{10} \leq 9.8 \text{ m s}^{-1}$, while DWLs only survived $U_{10} \leq 7.6 \text{ m s}^{-1}$ (99th percentile
731 values). RLs were also much less likely to occur when R_{MAX} decreased below 5 mm h^{-1} (**Fig. 8**),

732 which can explain the rare occurrence of RLs during suppressed MJO periods when $U_{10} < 8 \text{ m s}^{-1}$
733 ¹ but when sky conditions were mostly clear with little rain (**Fig. 6**). RLs and RL-DWLs were
734 most likely to occur during disturbed and active MJO periods, which exhibit frequent, heavy rain
735 and $U_{10} < 8\text{-}9 \text{ m s}^{-1}$ (**Table 1**) During WWBs, U_{10} was between $7\text{-}10 \text{ m s}^{-1}$, leading to only 2
736 observed RLs despite persistently high B from rainfall during this period (**Fig. 6, Fig. 8, Fig. 9**).
737 WWB conditions, characterized by both net surface cooling and high U_{10} , were even less suitable
738 for DWL formation: no DWLs were observed during WWB periods. Near-surface stratification
739 during WWB periods was also diminished by shear-driven turbulence generated from a Wyrтки
740 Jet in the upper 50-100 m (*Moum et al. 2014*). DWLs without RL influence were most common
741 in suppressed periods when strong net ocean heating occurred in conjunction with little rain and
742 light wind conditions ($U_{10} < 7 \text{ m s}^{-1}$ during 95% of suppressed periods, **Fig. 6**). DWLs also
743 occurred in disturbed and active periods, but 83% of these occurred in combination with RLs at
744 some point (**Table 2, Fig. 6, Fig. 9**).

745 The different phasing of DWL occurrence vs. RL occurrence relative to MJO evolution
746 could have implications for tropical air-sea interactions (*Zhang 2005, DeMott et al. 2014, 2015,*
747 *2016*). The influence of DWLs on ocean mixed layer temperature, SST, air-sea fluxes, and
748 precipitation in suppressed MJO periods has already been well-established in previous studies
749 (*Shinoda and Hendon 1998, Bellenger et al. 2010, Matthews et al. 2014, Seo et al. 2014, Chen et*
750 *al. 2015, Ruppert and Johnson 2015, 2016, Ruppert 2016, Johnson and Ciesielski 2017*).

751 Compared to DWLs alone, RLs and RL-DWLs occurred closer in time to the beginning of the
752 active MJO period, when the most intense atmospheric convection tends to occur, and also
753 occurred closer in time to WWB periods, when rain was more often stratiform (longer duration

754 and lighter intensity) and U_{10} was stronger (**Fig. 6**, atmospheric conditions as a function of MJO
755 phase discussed further in *Benedict and Randall 2007, Xu and Rutledge 2014*).

756 Rain's impact on near-surface ocean stability and mixing throughout the MJO should not
757 be ignored. Throughout the two MJOs, RLs created conditions during which turbulence was
758 limited to the upper few meters of the ocean rather than the seasonal mean mixed layer depth
759 described by CTD and Argo climatologies (**Fig. 9**). RLs were observed to form at least as often
760 as DWLs (32 vs. 30 events), several RLs were observed to persist locally for 10-14 h, and RLs
761 were observed at all times of the day and night (**Table 2, Fig. 6, Fig. 7**). Since RLs played a
762 significant role in establishing near-surface ocean stratification (occupying 16% of the dataset),
763 analysis of upper ocean stability based on temperature or DWLs alone is incomplete outside of
764 suppressed MJO periods.

765 Global investigations of RL coverage have not yet been completed. Similar to this study's
766 findings, RLs at other latitudes are also likely to cover smaller areas and shorter time period than
767 DWLs due to the localized area and short duration of rain events compared to the coverage of
768 cloud-free, low-wind conditions required to form DWLs. Large areas of tropical, subtropical, and
769 midlatitude oceans may be cloud-free at any given time. In contrast, rainfall is narrowly
770 concentrated across equatorial latitude bands due to the Intertropical Convergence Zone,
771 monsoons, and the MJO, as well as broadly distributed across the midlatitudes associated with
772 the passage of large low pressure systems (e.g. *Pendergrass and Deser 2017*). If the sensitivity
773 of RL formation and persistence to U_{10} is also considered, the global coverage and frequency of
774 RLs would be even lower than suggested by rain climatologies alone. This hypothesis was
775 confirmed by simulations conducted by *Drushka et al. (2016)* for tropical regions using a 1-D
776 turbulence-allowing ocean model and reanalysis data.

777 Results presented herein should motivate future studies regarding coupled numerical
778 models and observational analysis. The tendency for DWLs and RLs to coexist (16 continuous
779 events) and for overnight RLs to last into the next daytime cycle (4 events) suggests that
780 parameterizations for near-surface stratification should be designed so that RLs and DWLs can
781 form in the same place and evolve concurrently. Furthermore, RL formation and persistence was
782 strongly related to instantaneous rain rate, R , on 10-min time scales. Therefore, the accuracy of
783 predicted or assimilated rain on these timescales will impact the fidelity of simulated upper
784 ocean stratification in numerical models. Model mixing schemes will also determine the
785 simulated impacts of rain and surface warming on the ocean. Since RLs, DWLs, and their
786 combinations were typically between 2-4 m thick vertically with $h_S \leq 5$ m (**Fig. 4**), 1-m vertical
787 resolution in the upper 5-10 m appears critical for observational and modeling experiments
788 regarding RLs and DWLs. Argo floats, bathythermograph measurements, and most moorings
789 have historically observed S and T at 1-5 m depth with 2 m vertical resolution, which have not
790 consistently captured near-surface RLs or DWLs (*Gould et al. 2004, Anderson and Riser 2014*).
791 The frequent occurrence of RLs and DWLs in tropical oceans would also be completely ignored
792 in coupled model results that rely on mean or slab mixed layer depths. An MJO air-sea coupled
793 processes review by *DeMott et al. (2015)* does not recommend configuring coupled models with
794 mean or slab-ocean mixed layer depths. For instance, the DYNAMO stable layer depth, h_S , was
795 only within ± 5 m of the 20-m mean value of h_S for 9% of this dataset. The dominant modes of
796 variability in the upper Indian Ocean observed throughout 2 MJOs during DYNAMO can be
797 more accurately summarized in two ways (**Fig. 9**): (1) rain and/or diurnal heating stabilized the
798 upper 5 m of the ocean and limited wind-mixing to these shallow depths on 37/42 days, 38% of

799 the time; (2) turbulence and ocean convection mixed the water from the surface to at least 40 m
800 depth on 20/42 days, 62% of the time.

801 **6. Conclusions**

802 Near-surface ocean stable layers limit the penetration depth of wind-mixing and the
803 vertical distribution of atmospheric fluxes of momentum, freshwater, and heat. Therefore, the
804 presence of near-surface ocean stable layers can amplify both sea surface temperature and sea
805 surface salinity variability (SST and SSS). Leading up to this study, diurnal warm layers (DWLs)
806 resulting from surface heating were more comprehensively understood compared to rain layers
807 (RLs) resulting from precipitation; both RLs and DWLs are statically-stable near-surface layers.
808 While DWLs were known to frequent the low-wind, high-insolation suppressed period of the
809 Madden-Julian Oscillation (MJO), the frequency at which RLs or their combinations with DWLs
810 occurred throughout the MJO was unknown. The current study used central Indian Ocean ship-
811 based observations of rain, wind, and vertical gradients of ocean temperature and salinity to
812 better understand the following features of RLs, DWLs, and RL-DWLs: their formation and
813 persistence as a function of U_{10} and B, as well as their occurrence as a function of MJO phase.
814 Tracking of 30 DWLs, 32 RLs, and 17 RL-DWL combinations from a stationary research vessel
815 revealed that, throughout two MJO events:

- 816 • RLs and DWLs stabilized the upper 5 m of the ocean 38% of the time.
- 817 • Although RLs were more numerous than DWLs, 32 vs. 30 events, RLs existed about half as
818 often as DWLs. During 16% of the dataset, RLs of some kind occurred; in 30% of the dataset,
819 some form of DWLs occurred.
- 820 • RLs and RL-DWLs were observed with durations ≤ 14 and ≤ 11 h (mean duration = 5 h),
821 whereas DWLs were observed with longer durations ≤ 21 h (mean duration = 10 h).

- 822 ● RLs and RL-DWL combinations primarily formed in disturbed and active MJO conditions,
823 usually forming at least once per 24 hours in these periods.
- 824 ● DWLs without RL influence usually occurred daily in suppressed MJO conditions and
825 occurred rarely thereafter.
- 826 ● Of the DWLs that occurred in the disturbed and active MJO periods, all but one combined
827 with an RL at some point.
- 828 ● During westerly wind burst (WWB) conditions, DWLs did not form and RLs formed rarely.
- 829 ● When DWLs were present, 99% of U_{10} values were below 7.6 m s^{-1} . When RLs were present,
830 99% of U_{10} were below 9.8 m s^{-1} .
- 831 ● RLs contained enough buoyancy to withstand nocturnal ocean convection and surface
832 cooling. RLs forming during the day were often observed to persist through the day-to-night
833 transition. RLs forming at night were often observed to persist through the night-to-day
834 transition.
- 835 ● An estimate for stable layer depth, \hat{h}_S , was developed based on U_{10} and the buoyancy flux, B .
836 This led to an estimate for \hat{U}_S , the maximum U_{10} at which stable layers should exist at depth
837 h_S for fixed B . These stable layer estimation methods predicted 88% DWLs and RLs above 5
838 m depth within the same time span of observed stable layers, for 36 out of 44 total stable
839 layers.
- 840 ● RLs and RL-DWL combinations tended to occur in disturbed and active MJO periods,
841 whereas DWLs alone were more frequent in suppressed MJO periods. The different
842 occurrence rate of RLs vs. DWLs throughout the MJO cycle appears to be explained by
843 variations in Q_{Net} , R , and U_{10} throughout the MJO, and by the fact that RLs can withstand
844 higher U_{10} than DWLs.

- 845 • The 20-m mean value of stable layer depth, $\overline{h_S}$, was almost never observed, leading to over-
846 or under-estimation of the penetration depth of wind mixing in 91% of the dataset. Errors
847 were typically 100% or more. Similar errors were caused by monthly mean mixed layer
848 depths derived from climatologies of Argo profiles, which were similar to observed $\overline{h_S}$.
- 849 • The distribution of observed stable layer depth, h_S , was bi-modal, centered at 0-5 m during
850 near-surface stable layers or centered at 40-70 m when water was well-mixed from the surface
851 to the thermocline.

852 Near-surface stable layers are an important aspect of the coupled climate system because they
853 resist vertical mixing of water upward or downward across the stable layer and can thereby
854 influence SST, SSS, air-sea fluxes, and ocean heat content.

855

856 **7. Acknowledgements:**

857 This research was the focus of a PhD dissertation at Colorado State University (CSU)
858 Department of Atmospheric Science and was supported primarily by an interdisciplinary NSF
859 Graduate Research Fellowship Award DGE-1321845 (EJT) as well as NSF Award AGS-
860 1063928 (SAR), NSF Award OCE-1059055 (JNM). During the completion of this work, the first
861 author (EJT) was supported as a postdoctoral research associate at the Applied Physics
862 Laboratory at the University of Washington (APL-UW). The oceanographic experimental
863 support for this project provided by ONR Award N0001-10-1-2098 (JNM). C. W. Fairall's
864 participation in DYNAMO was partially funded by the NOAA Climate Program Office's ESS
865 division. Data access: http://data.eol.ucar.edu/master_list/?project=DYNAMO. We thank Paul
866 Hein (CSU) for data management. We also thank the Ocean Mixing Group at Oregon State
867 University (OSU) for collecting and providing all oceanographic data. We greatly appreciate

868 conversations with Eric D. Maloney, Richard H. Johnson, David A. Randall, Charlotte A.
 869 DeMott, and Douglas C. Stolz (CSU), Aurélie Moulin and Simon de Szoeko (OSU), as well as
 870 William E. Asher, Kyla Drushka, and Eric A. D’Asaro (APL-UW). William E. Asher made
 871 substantial contributions in regard to manuscript editing and the synthesis of research results.
 872 Suggestions from two anonymous reviewers improved the manuscript, and are gratefully
 873 acknowledged.

874

875 **Appendix A: Surface Buoyancy Flux into the Ocean**

876 From *Dorrestein (1979)*, the surface buoyancy flux into the ocean is

$$B = \frac{g}{\rho_W} \left[S_0 \beta (P - E) - \frac{\alpha}{c_P} (Q_{Lat} + Q_{Sens} + Q_{Solar} + Q_{IR}) + \alpha \Delta TP \right] \quad [11]$$

877	Rain Freshening	Heating	Rain Cooling
878	and Evaporation Term	Term	Term

879 **Table A1** explains the variables, constants, and typical values for components of B in [A1]. The
 880 first term of [A1] conveys how the precipitation mass flux, P , makes the surface layer more
 881 buoyant, i.e. less dense, whereas evaporation mass flux, E , increases surface salt content and
 882 therefore increases surface seawater density. The second term of [A1] describes the generation of
 883 buoyancy by surface heating (stabilization) and the destruction of buoyancy by surface cooling
 884 (destabilization). Similar to the heating term of [A1], the rain cooling term of [A1] accounts for
 885 surface heat loss and layer destabilization by the rain-sea temperature difference (*Gosnell et al.*
 886 *1995, Fairall et al. 1996b*).

887 To evaluate [A1], the rain rate, R , must be multiplied by the density of pure water, $\rho_{PW} =$
 888 1000 kg m^{-3} , to determine the precipitation mass flux, P , in $\text{kg m}^{-1} \text{ s}^{-1}$:

$$P = \rho_{PW}R \quad [12]$$

889 Similarly, the evaporation mass flux, E in $\text{kg m}^{-1} \text{s}^{-1}$, is determined by:

$$E = Q_{Lat}\rho_{PW}L_V^{-1} \quad [13]$$

890 where L_V is the latent heat of vaporization, 2.25×10^6 to 2.5×10^6 at 100°C to 0°C , respectively.

891 When evaluated with central Indian Ocean observations of fluxes, R , and surface water
 892 properties, B is widely distributed between -3×10^{-7} and 2×10^{-5} (**Fig. A1**). The most frequent
 893 values of B are negative, corresponding to persistent evaporation and cooling by the sensible,
 894 latent, and radiative heat fluxes (minimum $Q_{\text{Net}} = 400 \text{ W m}^{-2}$). The maximum rate of evaporation
 895 that was observed during DYNAMO was 0.6 mm h^{-1} , over two orders of magnitude lower than
 896 the maximum rain rate that was observed: 184 mm h^{-1} measured within 8 km upstream of the
 897 ship radar and 96 mm h^{-1} measured by the ship rain gauge. Compared to the net heat flux, rain
 898 produced values of B that were distributed over a wider range and were of much greater
 899 magnitude (**Fig. A1**). [A1] shows that equivalent B is produced by a median daily max heating
 900 rate of $Q_{\text{Net}} = -850 \text{ W m}^{-2}$ and relatively weak rain rate of $R = 10 \text{ mm h}^{-1}$. Maximum Q_{Net}
 901 observed during DYNAMO was -1035 W m^{-2} , which produced only slightly larger B (**Fig. A1**).

902 B due to interfacial turbulent/radiative heat exchanges, B_Q , can be systematically
 903 separated from B contributed by rain, B_R :

$$B = B_Q + B_R \quad [14]$$

$$B_R = \frac{g}{\rho_W} P(S_0\beta + \alpha\Delta T) \quad [15]$$

$$B_Q = \frac{g\alpha}{\rho_W c_P} \left[\left(1 - \frac{\beta c_P}{\alpha L_V} S_0 \right) Q_{Lat} + Q_{Sens} + Q_{Solar} + Q_{IR} \right] \quad [16]$$

904 B_Q and B_R are compared in **Fig 8**. The value of B_R is often over an order of magnitude greater
905 than the value of B_Q , yet instances of positive B_R are more episodic compared to the sinusoidal
906 manner of positive B_Q .

907 Evaluation of [A5] with central Indian observations from **Table A1** implies that the
908 stabilizing rain-freshening term, $S_0\beta$, is about 15 times the destabilizing rain-cooling term, $\alpha\Delta T$,
909 in [A5]. This means that the stabilizing effect of rain freshening on surface buoyancy is 15 times
910 larger than the destabilizing effect of rain cooling on surface buoyancy. Therefore, the effect of
911 rain cooling on B and B_R can be ignored. B_R is always a positive, stabilizing flux, as shown in
912 **Fig. 8** for the entire DYNAMO experiment.

913 The factor $\frac{\beta c_P}{\alpha L_V} S_0$ in [A6] is about 0.10 in the tropics using values from **Table A1**, so in
914 regard to B and B_Q , the effect of evaporative cooling is overwhelmingly larger than the effect of
915 evaporative salinification, which is also shown in **Table A1** and by *Asher et al. (2015)*.

916 Despite the fact that this study finds rain freshening to be responsible for greater B than
917 solar heating (**Fig. 8**), [A1] and [A6] actually overestimate the stabilizing effect of the net solar
918 flux (Q_{Solar}) because, unlike the net longwave flux (Q_{IR}) that is absorbed within the top 10 μm ,
919 Q_{Solar} is not entirely absorbed at the interface. Instead, roughly 50% of Q_{Solar} is absorbed within
920 the top 0.5 m and the remainder is absorbed over the top 5-9 m (see Table 3 in *Fairall et al.,*
921 *1996a*).

922

923 **Appendix B: Processing of Precipitation Radar Data**

924 The standard *Yuter and Houze (1998)* convective and stratiform radar echo partitioning
925 algorithm was applied to the Z_h field at the lowest vertical level, which was at 0.75 km above sea

926 level. The algorithm's tunable parameters were tested to produce the most physically-realistic
927 partitioning between convective and stratiform portions of storms in this dataset (*Steiner et al.*
928 *1995, Yuter and Houze 1998, Houze 1997, Schumacher et al. 2003, Thompson et al. 2015*).
929 Vertical cross sections of radar data were investigated during algorithm testing to ensure that
930 stratiform rain classification was only made where a clear, robust radar bright band was
931 occurring. Therefore, stratiform rain designations were only made when vertical profiles of radar
932 data indicated that a melting layer and stratiform rain microphysical processes were both
933 occurring. As part of the algorithm's standard procedures, background Z_h was smoothed about a
934 4 km radius of each grid point. The algorithm's climatological parameters were $a = 60$ and $b =$
935 100 . First, grid points were classified as convective when Z_h exceed the smoothed background Z_h
936 by 17 dBZ. Following standard procedures, neighboring grid points within 2, 3, 4, 5, and 6 km
937 range from these convective grid points were also classified as convective if Z_h exceeded the
938 following thresholds, respectively: 25 dBZ, 25-30 dBZ, 30-35 dBZ, 35-40 dBZ, and 40 dBZ.

939 In order to calculate R at each radar grid point, Z_h [dBZ] was first converted into linear
940 units, z [$\text{mm}^6 \text{m}^{-3}$] via: $z = 10^{(0.1 Z_h)}$. Then R was calculated at each grid point using two power
941 law estimators, one for convective points: $R = 0.0366 z^{0.684}$, and another for stratiform points: R
942 $= 0.0258 z^{0.644}$. These R estimators were developed by *Thompson et al. (2015)* for tropical
943 oceanic rainfall experienced over the IndoPacific Warm Pool. If radar echo partitioning into
944 convective and stratiform areas can be performed with confidence, using separate R estimators
945 for convective and stratiform rain can significantly reduce error associated with R estimation
946 (*Thompson et al. 2015*).

947

948 **References:**

- 949 Anderson, J. E. and S. C. Riser, 2014: Near-surface variability of temperature and salinity in the
950 near-tropical ocean: Observations from profiling floats. *J. Geophys. Res.*, **119**, 7433–
951 7448.
- 952 Anderson, S. P., R. A. Weller, and R. B. Lukas, 1996: Surface buoyancy forcing and the mixed
953 layer of the Western Pacific Warm Pool: Observations and 1D model results. *J. Climate*,
954 **9**, 3056–3085.
- 955 Asher, W. E., A. T. Jessup, R. Branch, and D. Clark, 2014: Observations of rain-induced near-
956 surface salinity anomalies. *J. Geophys. Res.*, **119**, 5483–5500.
- 957 Asher, W. E., A. T. Jessup, and D. Clark, 2015: Stable near-surface ocean salinity stratifications
958 due to evaporation observed during STRASSE. *J. Geophys. Res.*, **119**, 3219–3233.
- 959 Atlas, D., C. W. Ulbrich, F. D. Marks, Jr., E. Amitai, and C. R. Williams, 1999: Systematic
960 variation of drop size and radar-rainfall relations. *J. Geophys. Res.*, **104**, 6155–6169.
- 961 Back, L. E. and C. S. Bretherton, 2009a: On the relationship between SST gradients, boundary
962 layer winds, and convergence over the tropical oceans. *J. Climate*, **22**, 4182–4196.
- 963 Back, L. E. and C. S. Bretherton, 2009b: A simple model of climatological rainfall and vertical
964 motion patterns over the tropical oceans. *J. Climate*, **22**, 6477–6497.
- 965 Barnes, H. C. and R. A. Houze, Jr., 2013: The precipitating cloud population of the Madden-
966 Julian Oscillation over the Indian and west Pacific Oceans. *J. Geophys. Res.*, **118**, 6996–
967 7023.
- 968 Bellenger, H. and J.-P. Duvel, 2009: An analysis of tropical ocean diurnal warm layers. *J.*
969 *Climate*, **22**, 3629–3646.
- 970 Bellenger, H., Y. N. Takayabu, T. Ushiyama, and K. Yoneyama, 2010: Role of diurnal warm
971 layers in the diurnal cycle of convection over the tropical Indian Ocean during MISMO.
972 *Mon. Weather Rev.*, **138**, 2426–2433.
- 973 Benedict, J. J. and D. A. Randall, 2007: Observed characteristics of the MJO relative to
974 maximum rainfall. *J. Atmos. Sci.*, **64**, 2332–2354.
- 975 Boutin, J., N. Martin, G. Reverdin, X. Yin, and F. Gaillard, 2013: Sea surface freshening inferred
976 from SMOS and ARGO salinity: impact of rain. *Ocean Sci.*, **9**, 183–192.
- 977 Brainerd, K. E. and M. C. Gregg, 1995: Surface mixed and mixing layer depths. *Deep-Sea Res.*
978 *Pt. I*, **42**, 1521–1543.
- 979 Brainerd, K. E. and M. C. Gregg, 1997: Turbulence and stratification on the tropical ocean-
980 global atmosphere-coupled ocean-atmosphere response experiment microstructure pilot
981 cruise. *J. Geophys. Res.*, **102**, 10 437–10 455.
- 982 Carbone, R. E. and Y. Li, 2015: Tropical oceanic rainfall and sea surface temperature structure:
983 Parsing causation from correlation in the MJO. *J. Atmos. Sci.*, **72**, 2703–2718.
- 984 Chen, S., et al., 2015: A study of CINDY/DYNAMO MJO suppressed phase. *J. Atmos. Sci.*, **72**,
985 3755–3779.

- 986 Chi, N.-H., R.-C. Lien, E. A. D'Asaro, and B. B. Ma, 2014: The surface mixed layer heat budget
987 from mooring observations in the central Indian Ocean during Madden-Julian Oscillation
988 events. *J. Geophys. Res.*, **119**, 4638–4652.
- 989 Clayson, C. and L. Kantha, 1999: Turbulent Kinetic Energy and Its Dissipation Rate in the
990 Equatorial Mixed Layer. *J. Phys. Oceanogr.*, **29**, 2146–2166.
- 991 Clayson, C. and A. Bogdanoff, 2013: The Effect of Diurnal Sea Surface Temperature Warming
992 on Climatological Air–Sea Fluxes. *J. Climate*, **26**, 2546–2556.
- 993 Cronin, M. F. and M. J. McPhaden, 1997: The upper ocean heat balance in the western equatorial
994 Pacific warm pool during September–December 1992. *J. Geophys. Res.*, **102**, 8533–8553.
- 995 Cronin, M. F. and M. J. McPhaden, 1998: Upper ocean salinity balance in the Western
996 Equatorial Pacific. *J. Geophys. Res.*, **103**, 27 567–27 587.
- 997 Cronin, M. F. and M. J. McPhaden, 1999: Diurnal cycle of rainfall and surface salinity in the
998 western Pacific warm pool. *Geophys. Res. Lett.*, **26**, 3465–3468.
- 999 Costa, A. A., W. R. Cotton, R. L. Walko, and R. A. Pielke, 2001: Coupled ocean-cloud-resolving
1000 simulations of the air-sea interaction over the Equatorial Western Pacific. *J. Atmos. Sci.*,
1001 **58**, 3357–3375.
- 1002 Curry, J.A., A. Bentamy, M.A. Bourassa, D. Bourras, E.F. Bradley, M. Brunke, S. Castro, S.H.
1003 Chou, C.A. Clayson, W.J. Emery, L. Eymard, C.W. Fairall, M. Kubota, B. Lin, W.
1004 Perrie, R.A. Reeder, I.A. Renfrew, W.B. Rossow, J. Schulz, S.R. Smith, P.J. Webster,
1005 G.A. Wick, and X. Zeng, 2004: SEAFLUX. *Bull. Amer. Meteor. Soc.*, **85**, 409–424
- 1006 de Boyer Montégut, C., G. Madec, A. S. Fischer, A. Lazar, and D. Iudicone, 2004: Mixed layer
1007 depth over the global ocean: An examination of profile data and a profile-based
1008 climatology. *J. Geophys. Res.*, **109**, C12.
- 1009 de Szoeké, S. P., J. B. Edson, J. R. Marion, C. W. Fairall, and L. Bariteau, 2014: The MJO and
1010 air-sea interaction in TOGA COARE and DYNAMO. *J. Climate*, **28**, 597–622.
- 1011 de Szoeké, S.P., E.D. Skillingstad, P. Zuidema, and A.S. Chandra, 2017: Cold Pools and Their
1012 Influence on the Tropical Marine Boundary Layer. *J. Atmos. Sci.*, **74**, 1149–1168
- 1013 DeMott, C.A., C. Stan, D.A. Randall, and M.D. Branson, 2014: Intraseasonal Variability in
1014 Coupled GCMs: The Roles of Ocean Feedbacks and Model Physics. *J. Climate*, **27**,
1015 4970–4995.
- 1016 DeMott, C. A., N. P. Klingaman, and S. J. Woolnough, 2015: Atmosphere-ocean coupled
1017 processes in the Madden-Julian oscillation. *Rev. Geophys.*, **53**, 1099–1154.
- 1018 DeMott, C. A., J. J. Benedict, N. P. Klingaman, S. J. Woolnough, and D. A. Randall (2016),
1019 Diagnosing ocean feedbacks to the MJO: SST-modulated surface fluxes and the moist
1020 static energy budget, *J. Geophys. Res. Atmos.*, **121**, 8350–8373
- 1021 Dorrestein, R., 1979: On the vertical buoyancy flux below the sea surface as induced by
1022 atmospheric factors. *J. Phys. Oceanogr.*, **9**, 229–231.

- 1023 Drushka, K., J. Sprintall, S. T. Gille, and S. Wijffels, 2012: In situ observations of Madden-
1024 Julian Oscillation mixed layer dynamics in the Indian and Western Pacific Oceans. *J.*
1025 *Climate*, **25**, 2306–2328.
- 1026 Drushka, K., W. E. Asher, B. Ward, and K. Walesby, 2016: Understanding the formation and
1027 evolution of rain-formed fresh lenses at the ocean surface, *J. Geophys. Res. Oceans*, **121**,
1028 2673–2689, doi:10.1002/2015JC011527.
- 1029 Edson, J. B., et al., 2013: On the exchange of momentum over the open ocean. *J. Phys.*
1030 *Oceanogr.*, **43**, 1589–1610.
- 1031 Fairall, C. W., E. F. Bradley, J. S. Godfrey, G. A. Wick, J. B. Edson, and G. S. Young, 1996a:
1032 Cool-skin and warm-layer effects on sea surface temperature. *J. Geophys. Res.*, **101**,
1033 1295–1308.
- 1034 Fairall, C. W., E. F. Bradley, D. P. Rogers, J. B. Edson, and G. S. Young, 1996b: Bulk
1035 parameterization of air-sea fluxes for Tropical Ocean- Global Atmosphere Coupled-
1036 Ocean Atmosphere Response Experiment. *J. Geophys. Res.*, **101**, 3747–3764.
- 1037 Fairall, C. W., A. B. White, J. B. Edson, and J. E. Hare, 1997: Integrated shipboard
1038 measurements of the marine boundary layer. *Journal of Atmospheric and Oceanic*
1039 *Technology*, **14**, 338–359
- 1040 Fairall, C. W., E. F. Bradley, J. E. Hare, A. A. Grachev, and J. B. Edson, 2003: Bulk
1041 parameterization of air-sea fluxes: Updates and verification for the COARE algorithm. *J.*
1042 *Climate*, **16**, 571–591.
- 1043 Gosnell, R., C. W. Fairall, and P. J. Webster, 1995: The sensible heat of rainfall in the tropical
1044 ocean. *J. Geophys. Res.*, **100**, 18 437–18 442.
- 1045 Gottschalck, J., P. E. Roundy, C. J. S. III, A. Vintzileos, and C. Zhang, 2013: Large-scale
1046 atmospheric and oceanic conditions during the 2011–2012 DYNAMO field campaign.
1047 *Mon. Weather Rev.*, **141**, 4173–4196.
- 1048 Gray, W. M. and R. W. Jacobson, Jr., 1977: Diurnal variation of deep cumulus convection.
1049 *Mon. Wea. Rev.*, **105**, 1171–1188.
- 1050 Harrison, D. E., and G. A. Vecchi, 1997: Westerly wind events in the tropical Pacific, 1986–95.
1051 *J. Climate*, **10**, 3131–3156.
- 1052 Holte, J. and L. Talley, 2009: A New Algorithm for Finding Mixed Layer Depths with
1053 Applications to Argo Data and Subantarctic Mode Water Formation. *J. Atmos. Oceanic*
1054 *Technol.*, **26**, 1920–1939, <https://doi.org/10.1175/2009JTECHO543.1>
- 1055 Holte, J., L. D. Talley, J. Gilson, and D. Roemmich, 2017. An Argo mixed layer climatology and
1056 database, *Geophys. Res. Lett.*, **44**, 5618–5626, doi:10.1002/2017GL073426.
- 1057 Houze, R. A., Jr., 1997: Stratiform precipitation in regions of convection: A meteorological
1058 paradox? *Bull. Am. Meteorol. Soc.*, **78**, 2179–2196.
- 1059 Houze, R. A., Jr., K. L. Rasmussen, M. D. Zuluaga, and S. R. Brodzik, 2015: The variable nature
1060 of convection in the tropics and subtropics: A legacy of 16 years of the Tropical Rainfall
1061 Measuring Mission satellite, *Rev. Geophys.*, **53**, 994–1021.

- 1062 Johnson, R. and P. Ciesielski, 2013: Structure and properties of Madden-Julian Oscillations
1063 deduced from DYNAMO sounding arrays. *J. Atmos. Sci.*, **70**, 3157–3179.
- 1064 Johnson, R. H., T. M. Rickenbach, S. A. Rutledge, P. E. Ciesielski, and W. H. Schubert, 1999:
1065 Trimodal characteristics of tropical convection. *J. Climate*, **12**, 2397–2418.
- 1066 Kara, A. B., P. A. Rochford, and H. E. Hurlburt, 2000a: Mixed layer depth variability over the
1067 global ocean. *J. Geophys. Res.*, **108**, 0.
- 1068 Kara, A. B., P. A. Rochford, and H. E. Hurlburt, 2000b: An optimal definition for ocean mixed
1069 layer depth. *J. Geophys. Res.*, **105**, 16 803–16 821.
- 1070 Kara, A. B., P. A. Rochford, and H. E. Hurlburt, 2003: Mixed layer depth variability and barrier
1071 layer formation over the North Pacific Ocean. *J. Geophys. Res.*, **105**, 16 783–16 801.
- 1072 Kawai, Y. and A. Wada, 2007: Diurnal sea surface temperature variation and its impact on the
1073 atmosphere and ocean: A review. *Oceanography*, **63**, 721–744.
- 1074 Kiladis G. N., K. H. Straub and P. T. Haertel, 2005: Zonal and vertical structure of the Madden-
1075 Julian Oscillation. *J. Atmos. Sci.*, **62**, 2790–2809.
- 1076 Kilpatrick, T., and S.-P. Xie, 2016: Circumventing rain-related errors in scatterometer wind
1077 observations, *J. Geophys. Res. Atmospheres*, **121**, 9422–9440.
- 1078 Klingaman, N. P., S. J. Woolnough, H. Weller, and J. M. Slingo, 2011: The impact of finer-
1079 resolution air-sea coupling on the intraseasonal oscillation of the Indian summer
1080 monsoon. *J. Clim.*, **24**, 2451–2468.
- 1081 Klingaman, N. P., and S. J. Woolnough, 2014: The role of air-sea coupling in the simulation of
1082 the Madden-Julian oscillation in the Hadley Centre model, *Q. J. R. Meteorol. Soc.*, **140**,
1083 2272–2286.
- 1084 Kraus, E. B. and J. A. Businger, 1994: *Atmosphere-Ocean Interactions*. New York, Oxford
1085 University Press.
- 1086 Lau, W. K. M. and D. E. Waliser, 2005: *Intraseasonal Variability of the Atmosphere-Ocean*
1087 *Climate System*. Springer, Heidelberg, Germany, pp. 474 pp.
- 1088 Li, Y. and R. E. Carbone, 2012: Excitation of rainfall over the tropical Western Pacific.
1089 *J. Atmos. Sci.*, **69**, 2983–2994. Lindzen, R. and S. Nigam, 1987: On the role of sea
1090 surface temperature gradients in forcing low level winds and convergence in the tropics.
1091 *J. Atmos. Sci.*, **44**, 2418–2436.
- 1092 Lombardo, C. P. and M. C. Gregg, 1989: Similarity scaling of viscous and thermal dissipation in
1093 a convecting surface boundary layer. *J. Geophys. Res.*, **94**, 6273–6284.
- 1094 Lukas, R. and E. Lindstrom, 1991: The mixed layer of the Western Equatorial Pacific Ocean. *J.*
1095 *Geophys. Res.*, **96**, 3343–335.
- 1096 Madden, R. A. and P. R. Julian, 1994: Observations of the 40-50-day tropical oscillation-a
1097 review. *Mon. Weather Rev.*, **122**, 814–837.
- 1098 Matthews, A. J., D. B. Baranowski, K. J. Heywood, P. J. Flatau, and S. Schmidtko, 2014: The
1099 surface diurnal warm layer in the Indian Ocean during CINDY/DYNAMO. *J. Climate*,
1100 **27**, 1658–1672.

- 1101 McDougall, T.J. and P.M. Barker, 2011: Getting started with TEOS-10 and the Gibbs Seawater
 1102 (GSW) Oceanographic Toolbox, 28pp., SCOR/IAPSO WG127, ISBN 978-0-646-55621-
 1103 5.
- 1104 McPhaden, M. J. and G. R. Foltz, 2013: Intraseasonal variations in the surface layer heat balance
 1105 of the central equatorial Indian Ocean: The importance of zonal advection and vertical
 1106 mixing. *J. Geophys. Res.*, **40**, 2737–2741.
- 1107 Miller, J., 1976: The salinity effect in a mixed layer ocean model. *J. Phys. Oceanogr.*, **6**, 29–35.
- 1108 Moulin, A.J., J.N. Moum and E.L. Shroyer, 2017. Evolution of turbulence in the diurnal warm
 1109 layer. *J. Phys. Oceanogr.*, **48**, 383-396.
- 1110 Moum, J.N., M.C. Gregg, R.C. Lien and M.E. Carr, 1995. Comparison of turbulent kinetic
 1111 energy dissipation rates from two ocean microstructure profilers, *J. Oceanic Atmos.*
 1112 *Technol.*, **12**, 346–366.
- 1113 Moum, J. N., et al., 2014: Air-sea interactions from MJO westerly wind bursts. *Bull. Am.*
 1114 *Meteorol. Soc.*, **95**, 1185–1199.
- 1115 Pendergrass, A.G. and C. Deser, 2017: Climatological Characteristics of Typical Daily
 1116 Precipitation. *J. Climate*, **30**, 5985–6003, <https://doi.org/10.1175/JCLI-D-16-0684.1>
- 1117 Praveen Kumar, B., J. Vialard, M. Lengaigne, V. S. N. Murty, M. J. McPhaden, 2012: TropFlux:
 1118 air-sea fluxes for the global tropical oceans - description and evaluation. *Clim. Dyn.*, **38**,
 1119 1521.
- 1120 Price, J. F., 1979: Observations of a rain-formed mixed layer. *J. Phys. Oceanogr.*, **9**, 643–649.
- 1121 Price, J. F., R. A. Weller, and R. Pinkel, 1986: Diurnal cycling: Observations and models of the
 1122 upper ocean response to diurnal heating, cooling, and wind mixing. *J. Geophys. Res.*, **91**,
 1123 8411–8427.
- 1124 Prytherch, J., J. T. Farrar, and R. A. Weller, 2013: Moored surface buoy observations of the
 1125 diurnal warm layer. *J. Geophys. Res.*, **118**, 4553–4569.
- 1126 Randall, D. A., Harshvardhan, and D. A. Dazlich, 1991: Diurnal variability of the hydrologic
 1127 cycle in a general circulation model. *JAS*, **26**, 4062.
- 1128 Rickenbach, T. M. and S. A. Rutledge, 1988: Convection in TOGA COARE: Horizontal scale,
 1129 morphology, and rainfall production. *J. Atmos. Sci.*, **55**, 2715–2729.
- 1130 Rowe, A. K. and R. A. Houze, Jr., 2015: Cloud organization and growth during the transition
 1131 from suppressed to active MJO conditions. *J. Geophys. Res.*, **120**, 10 324–10 350.
- 1132 Ruppert, J. H. and R. H. Johnson, 2015: Diurnally modulated cumulus moistening in the pre-
 1133 onset stage of the Madden-Julian Oscillation during DYNAMO. *J. Atmos. Sci.*, **72**,
 1134 1622–1647.
- 1135 Sakaeda, N., S.W. Powell, J. Dias, and G.N. Kiladis, 2018: The Diurnal Variability of
 1136 Precipitating Cloud Populations during DYNAMO. *J. Atmos. Sci.*, **75**, 1307–1326.
- 1137 Santos-Garcia, A., M. M. Jacob, W. L. Jones, W. E. Asher, Y. Hejazin, H. Ebrahimi, and M.
 1138 Rabolli, 2014: Investigation of rain effects on Aquarius Sea Surface Salinity
 1139 measurements. *J. Geophys. Res. Oceans*, **119**, 7605–7624

1140 Schmidtko, S., G. C. Johnson, and J. M. Lyman, 2013: A global monthly isopycnal upper-ocean
1141 climatology with mixed layers. *J. Geophys. Res.*, **118**, 1658–1672.

1142 Seo, H., A. C. Subramanian, A. J. Miller, and N. R. Cavanaugh, 2014: Coupled impacts of the
1143 diurnal cycle of sea surface temperature on the Madden-Julian Oscillation. *J. Climate*, **27**,
1144 8422–8443.

1145 Smyth, W. D., D. Hebert, and J. N. Moum, 1996a: Local ocean response to a multiphase
1146 westerly wind burst: 1. dynamic response. *J. Geophys. Res.*, **101**, 22 495–22 512.

1147 Smyth, W. D., D. Hebert, and J. N. Moum, 1996b: Local ocean response to a multiphase
1148 westerly wind burst: 2. thermal and freshwater responses. *J. Geophys. Res.*, **101**, 22 513–
1149 22 533.

1150 Soloviev, A. and R. Lukas, 2006: *The Near-Surface Layer of the Ocean: Structure, Dynamics*
1151 *and Applications*. Springer, Netherlands, pp. 574 pp.

1152 Soloviev, A. and N. Vershinsky, 1982: The vertical structure of the thin surface layer of the
1153 ocean under conditions of low wind speed. *Deep Sea Res.*, **29**, 1437–1449.

1154 Soloviev, A., S. Matt, and A. Fujimura, 2015: Three-dimensional dynamics of fresh water lenses
1155 in the ocean’s near-surface layer. *Oceanography*, **28**, 142–149

1156 Stuart-Menteth, A. C., I. S. Robinson, and P. G. Challenor, A global study of diurnal warming
1157 using satellite-derived sea surface temperature, *J. Geophys. Res.*, **108**(C5), 3155,
1158 doi:10.1029/2002JC001534, 2003

1159 Sui, C.-H., X. Li, and K.-M. Lau, 1998: Radiative-convective processes in simulated diurnal
1160 variations of tropical oceanic convection. *J. Atmos. Sci.*, **55**, 2345–2357.

1161 Sui, C.-H., X. Li, K.-M. Lau, and D. Adamec, 1997: Diurnal variations in tropical oceanic
1162 cumulus convection during TOGA COARE. *Mon. Weather Rev.*, **125**, 448–462.

1163 Thompson, E. J., S. A. Rutledge, B. Dolan, and M. Thurai, 2015: Drop size distributions and
1164 radar observations of convective and stratiform rain over the equatorial Indian and west
1165 Pacific Oceans. *J. Atmos. Sci.*, **72**, 4091–4125.

1166 Webster, P. J., C. A. Clayson, and J. A. Curry, 1996: Clouds, radiation, and the diurnal cycle of
1167 sea surface temperature in the tropical Western Pacific. *J. Climate*, **9**, 1712–1730.

1168 Wheeler, M. C. and H. H. Hendon, 2004: An all-season real-time multivariate MJO index:
1169 Development of an index for monitoring and prediction. *Mon. Weather Rev.*, **132**, 1917–
1170 1932.

1171 Wijesekera, H. W. and M. C. Gregg, 1996: Surface layer response to weak winds, westerly
1172 bursts, and rain squalls in the western Pacific warm pool. *J. Geophys. Res.*, **101**, 977–997.

1173 Wijesekera, H. W., C. A. Paulson, and A. Huyer, 1999: The effect of rainfall on the surface layer
1174 during a westerly wind burst in the western equatorial Pacific. *J. Geophys. Res.*, **29**, 612–
1175 632.

1176 Woolnough, S. J., J. M. Slingo, and B. J. Hoskins, 2000: The relationship between convection
1177 and sea surface temperature on intraseasonal timescales. *J. Climate*, **13**, 2086–2104.

- 1178 Woolnough, S. J., J. M. Slingo, and B. J. Hoskins, 2001: The organization of tropical convection
1179 by intraseasonal sea surface temperature anomalies. *Q. J. R. Meteorol. Soc.*, **127**, 887–
1180 907.
- 1181 Xu, W. and S. A. Rutledge, 2014: Convective characteristics of the Madden-Julian Oscillation
1182 over the Central Indian Ocean Observed by Shipborne Radar during DYNAMO. *J.*
1183 *Atmos. Sci.*, **71**, 2859–2877.
- 1184 Xu, W. and S. A. Rutledge, 2015: Morphology, intensity, and rainfall production of MJO
1185 convection: Observations from DYNAMO and TRMM. *J. Atmos. Sci.*, **72**, 623–640.
- 1186 Yang, G.-Y. and J. Slingo, 2001: The diurnal cycle in the tropic. *Mon. Weather Rev.*, **129**, 784–
1187 801.
- 1188 Yoneyama, K., C. Zhang, and C. N. Long, 2013: Tracking pulses of the Madden-Julian
1189 oscillation. *Bull. Am. Meteorol. Soc.*, **94**, 1871–1891.
- 1190 You, Y., 1995: Salinity variability and its role in the barrier-layer formation during TOGA-
1191 COARE. *J. Phys. Oceanogr.*, **25**, 27782807.
- 1192 Yuter, S. and R. A. Houze, Jr., 1998: The natural variability of precipitating clouds over the
1193 Western Pacific Warm Pool. *Q. J. Roy. Met. Soc.*, **124**, 53–99.
- 1194 Zhang, C., 2005: Madden-Julian Oscillation. *Rev. Geophys.*, **43**, RG2003.
- 1195 Zhang, C. and M. J. McPhaden, 2000: Intraseasonal surface cooling in the Equatorial Western
1196 Pacific. *J. Climate*, **13**, 2261–2276.
- 1197 Zhang, C., 2013: Madden–Julian Oscillation: Bridging Weather and Climate. *Bull. Amer.*
1198 *Meteor. Soc.*, **94**, 1849–1870, <https://doi.org/10.1175/BAMS-D-12-00026.1>

1199 **Table 1: Meteorological conditions during two MJOs observed during this DYNAMO**
1200 **dataset.**
1201 MJO conditions at R/V *Revelle* location (80.5°E, 0°) according to Wheeler and Hendon (2004)
1202 RMM Index (<http://www.bom.gov.au/climate/mjo/graphics/rmm.74toRealtime.txt>). Time
1203 periods defined in this study start or end at 00Z except when denoted by superscript # = 08Z; @
1204 = 10Z; \$ = 17Z; % = 22Z. Two WWB pulses occurred during the November active MJO phase.
1205 Mean rain rate and wind speed calculated from *Revelle* gauge measurements. Sign convention
1206 for net heat flux is negative into the ocean (heating the ocean); positive out of the ocean (cooling
1207 the ocean). The mean daytime minimum value and mean daytime value of net heat flux, Q_{Net} ,
1208 were tracked. Daytime hours were considered to be 7 AM – 5 PM LST, 1-11 UTC. *The
1209 DYNAMO time periods in which complete vertical profiles of the ocean were measured at
1210 *Revelle* did not span all phases of the RMM index. Observation days did not include phases 4, 5,
1211 or 6. Observations were also not collected on all days of phases 7 or 3 (see **Sec. 2.1** for details).
1212

	MJO time period				
	suppressed (14 days)	disturbed (12 days)	active (10 days)	westerly wind burst (WWB, 6 days)	total (42 days)
RMM Index	7*-8	1	2-3*	2-3 when $U_{10} > 7 \text{ m s}^{-1}$	1-8*
time sampled while <i>Revelle</i> at 80.5°E, 0°	05-14 Oct 12-17 Nov	14-20 [%] Oct 17-21 [%] Nov	20 [@] -27 [@] Oct 21 [#] -24 [#] Nov 27- 27 ^{\$} Nov	27 [@] -28 Oct 24 [#] -27 Nov 27 ^{\$} -29 Nov	05-28 Oct 12-29 Nov
max R , mm h^{-1}	19	65	74	69	74
mean R , mm h^{-1}	0.03	0.28	0.51	1.45	0.42
99% U_{10} , m s^{-1}	7.9	8.1	9.1	15.9	13.1
mean U_{10} , m s^{-1}	4.1	2.7	4.1	9.1	4.3
mean of daytime min Q_{Net} , W m^{-2}	-855	-824	-732	-558	-775
mean of daytime Q_{Net} , W m^{-2}	-540	-386	-272	-20	-363

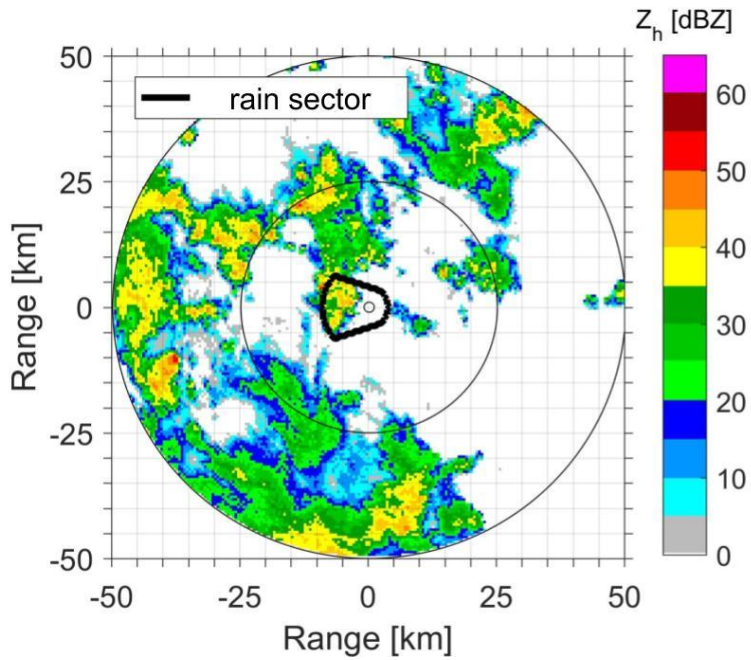
1213 **Table 2: Stable layers observed throughout two MJO lifecycles.**
 1214 Count of observed stable layers in each MJO period defined relative to the central Indian Ocean
 1215 (Table 1). The continuous stable layer event category counts events in which multiple RLs
 1216 and/or DWLs were present at the same time as a single continuous event. Events in which RLs
 1217 and DWLs combined occurred 18 individual times but contributed to only 16 continuous stable
 1218 layer events because 2 RL-DWL events were contained within preexisting stable events in which
 1219 another RL-DWL was also present. The total number of continuous stable layers is equal to the
 1220 sum of stable layers in RL-only, DWL-Only, and RL-DWL categories.
 1221

		MJO time period				total (42 days)
		suppressed (14 days)	disturbed (12 days)	active (10 days)	westerly wind burst (WWB, 6 days)	
stable layer count	RL-only	0	7	5	2	14
	DWL-only	11	2	1	0	14
	RL-DWL combo	2	8	6	0	16
	all RLs	2	16	12	2	32
	all DWLs	13	10	7	0	30
	continuous stable layer events	13	17	12	2	44

1222 **Table A1: Components of the surface buoyancy flux into the ocean.**
 1223 Variables, constants, and values for components of the ocean surface buoyancy flux B [A1]
 1224 evaluated with DYNAMO data from the current study. Heat fluxes, Q , are defined negative into
 1225 the ocean.
 1226

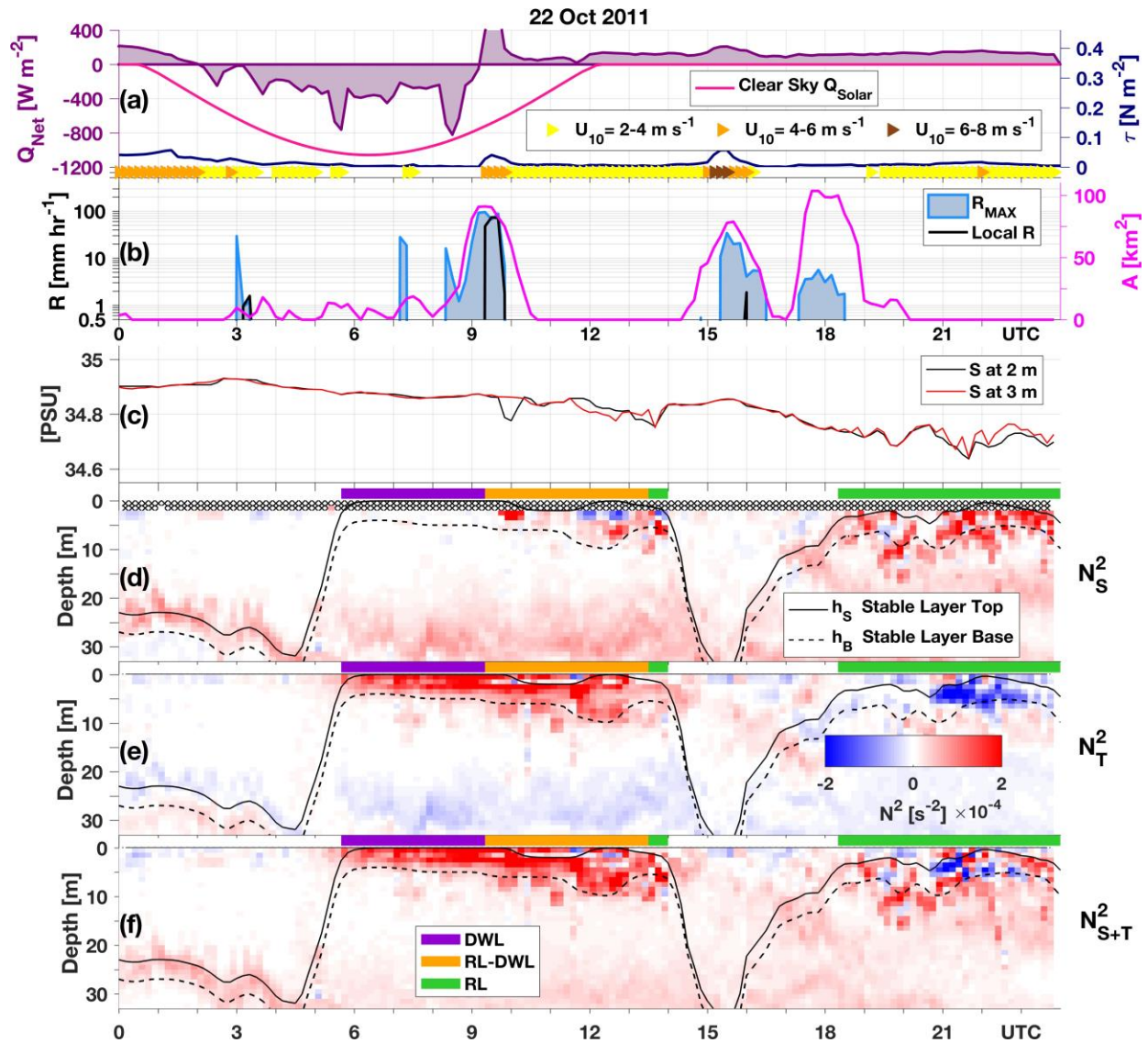
Name	Term	Value
gravitational constant	g	9.81 m s^{-2}
seawater density	ρ_w	1022 kg m^{-3}
sea surface salinity	SSS	33.7 to 35.5 PSU
sea surface temperature	SST	28.5 to 32.0 °C
Precipitation mass flux	P	0 to $0.0936 \text{ kg m}^{-2} \text{ s}^{-1}$
Evaporation mass flux	E	9×10^{-6} to $2 \times 10^{-4} \text{ kg m}^{-2} \text{ s}^{-1}$
thermal expansion coefficient	α	3.2×10^{-4} to $3.5 \times 10^{-4} \text{ }^\circ\text{C}^{-1}$
salt contraction coefficient	β	7.32×10^{-4} to $7.35 \times 10^{-4} \text{ PSU}^{-1}$
specific heat of seawater	c_p	3997 to $4007 \text{ J K}^{-1} \text{ kg}^{-1}$
latent heat flux	Q_{Lat}	22 to 410 W m^{-2}
sensible heat flux	Q_{Sens}	-0.5 to 100 W m^{-2}
net solar heat flux	Q_{Solar}	-1200 to 0 W m^{-2}
net infrared heat flux	Q_{IR}	18 to 77 W m^{-2}
rain-sea temperature difference	$\Delta T = T_w - \text{SST}$	-2.3 to $-6.9 \text{ }^\circ\text{C}$
wet bulb temperature	T_w	23.3 to $26.3 \text{ }^\circ\text{C}$
rain freshening and evaporation term	$S_0 \beta (P - E)$	-2.6×10^{-6} to $2.4 \times 10^{-3} \text{ kg m}^{-2} \text{ s}^{-1}$
heating term	$-(\alpha/c_p) Q_{\text{Net}}$	-4.4×10^{-5} to $8.7 \times 10^{-5} \text{ kg m}^{-2} \text{ s}^{-1}$
rain cooling term	$\alpha P \Delta T$	-1.3×10^{-4} to $0 \text{ kg m}^{-2} \text{ s}^{-1}$
first term	$g \rho_w^{-1}$	$9.6 \times 10^{-3} \text{ kg}^{-1} \text{ m}^4 \text{ s}^{-2}$
total buoyancy flux	B	-1.2×10^{-7} to $8.8 \times 10^{-6} \text{ m}^2 \text{ s}^{-3}$

1227
 1228
 1229
 1230



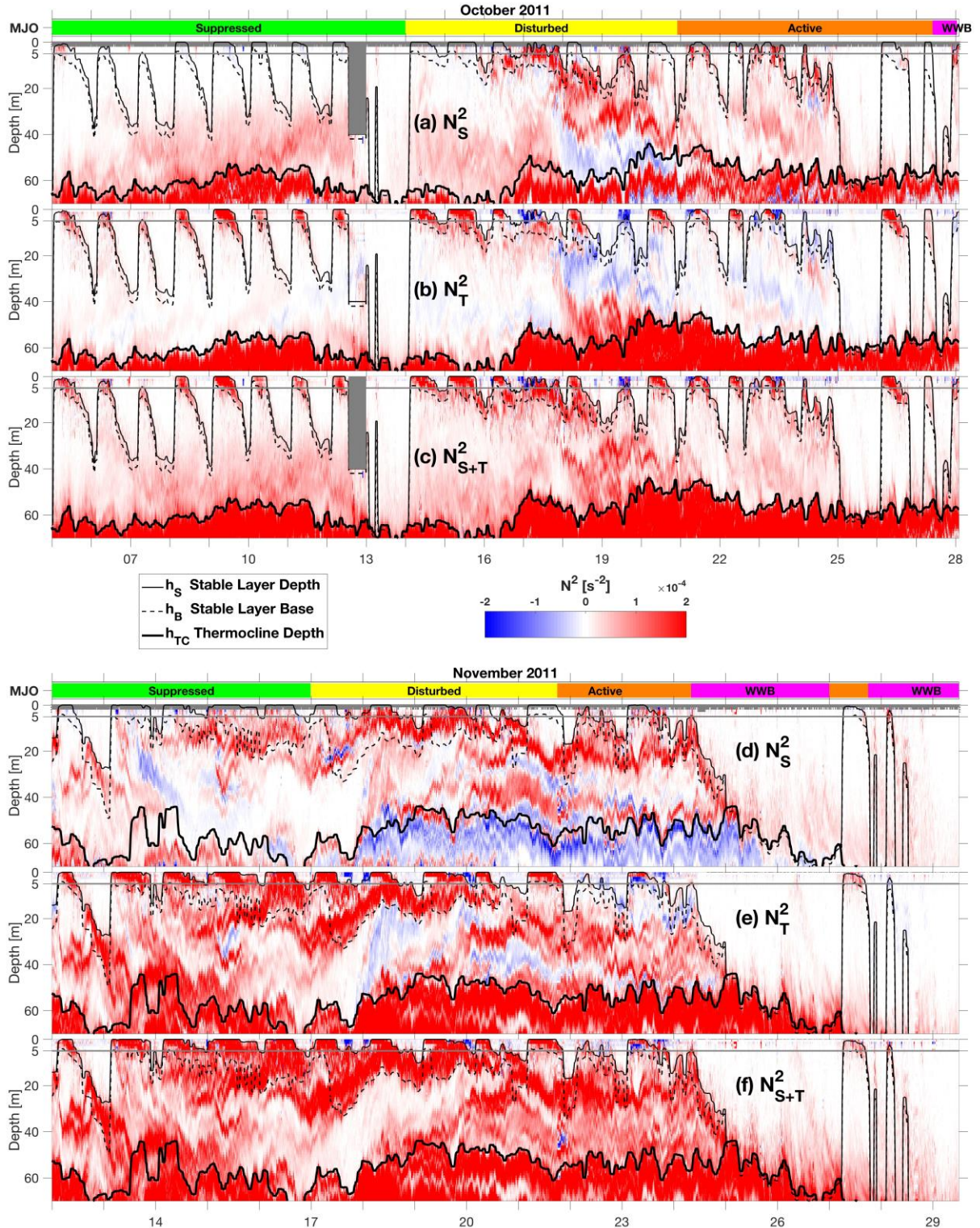
1231
 1232
 1233
 1234
 1235
 1236
 1237
 1238

Figure 1: R/V *Revelle* (0°, 80.5°E, position denoted by center circle) radar reflectivity (Z_h) with outline of rain sector area (thick black line). The sector extends 9 km from *Revelle* in the upstream direction and within 4 km of *Revelle* in all other directions. The upstream extension of the sector accounts for surface advection of rainwater within approximately the last 3 h by the mean 0.8 m s^{-1} eastward current during these cruises.



1239
1240

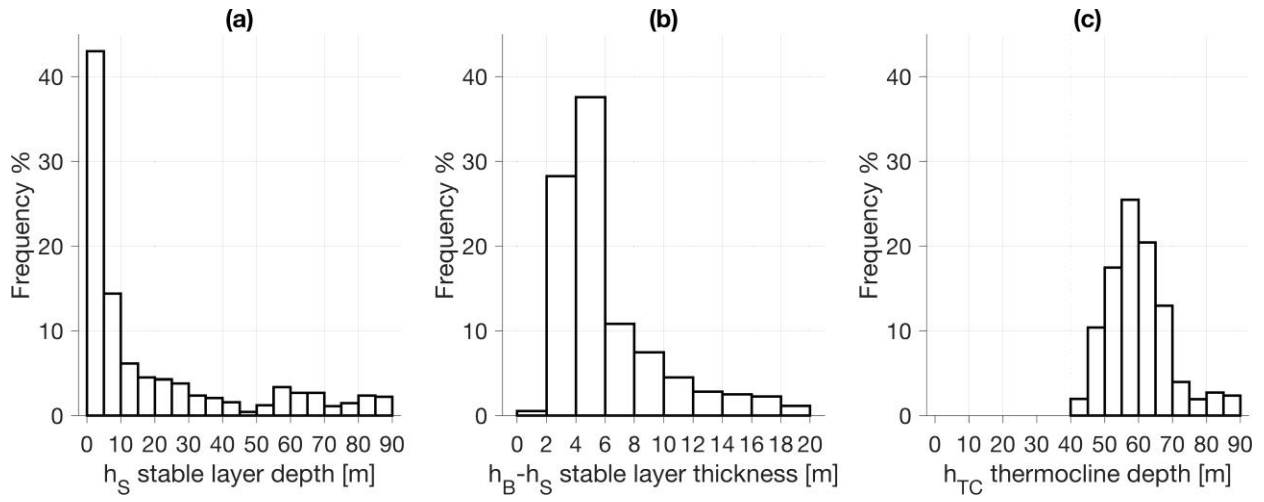
1241 **Figure 2:** 22 October 2011 case study of a DWL, a RL, and a RL-DWL combination (colored
1242 bars on top of (d, e, f): (a) net heat flux, Q_{Net} , modeled solar heat flux for clear-sky conditions,
1243 Q_{Solar} , wind stress, τ , and triangles color-coded by U_{10} ; (b) R observed locally at the research ship
1244 or the max value observed either locally or within the upstream radar sector, R_{MAX} , and the area,
1245 A , of the radar sector that was filled by rain echoes; (c) 2-m, and 3-m S from Chameleon profiler;
1246 (d) N_S^2 ; (e) N_T^2 ; (f) N_{S+T}^2 . Solid and dashed lines in (d-f) indicate the depth of the stable layer
1247 top, h_S , and the depth of the stable layer base, h_B .



1248
 1249
 1250
 1251
 1252
 1253

Figure 3: Observed N^2 due to S (a, d), T (b, e), S and T (c, f) as a function of depth and time during two equatorial, central Indian Ocean cruises. The depth of the stable layer, h_S , stable layer base, h_B , and thermocline, h_{TC} , were determined by the total N^2 field (c, f). The 5-m level is marked for reference.

1254



1255

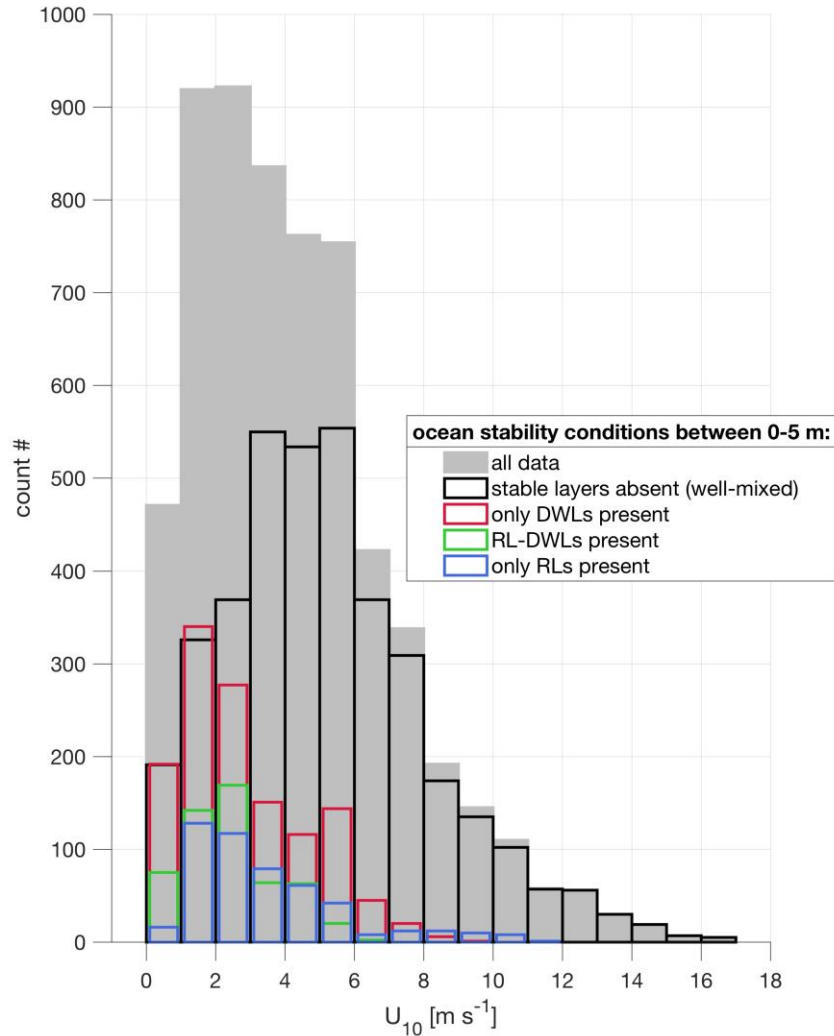
1256

1257

1258

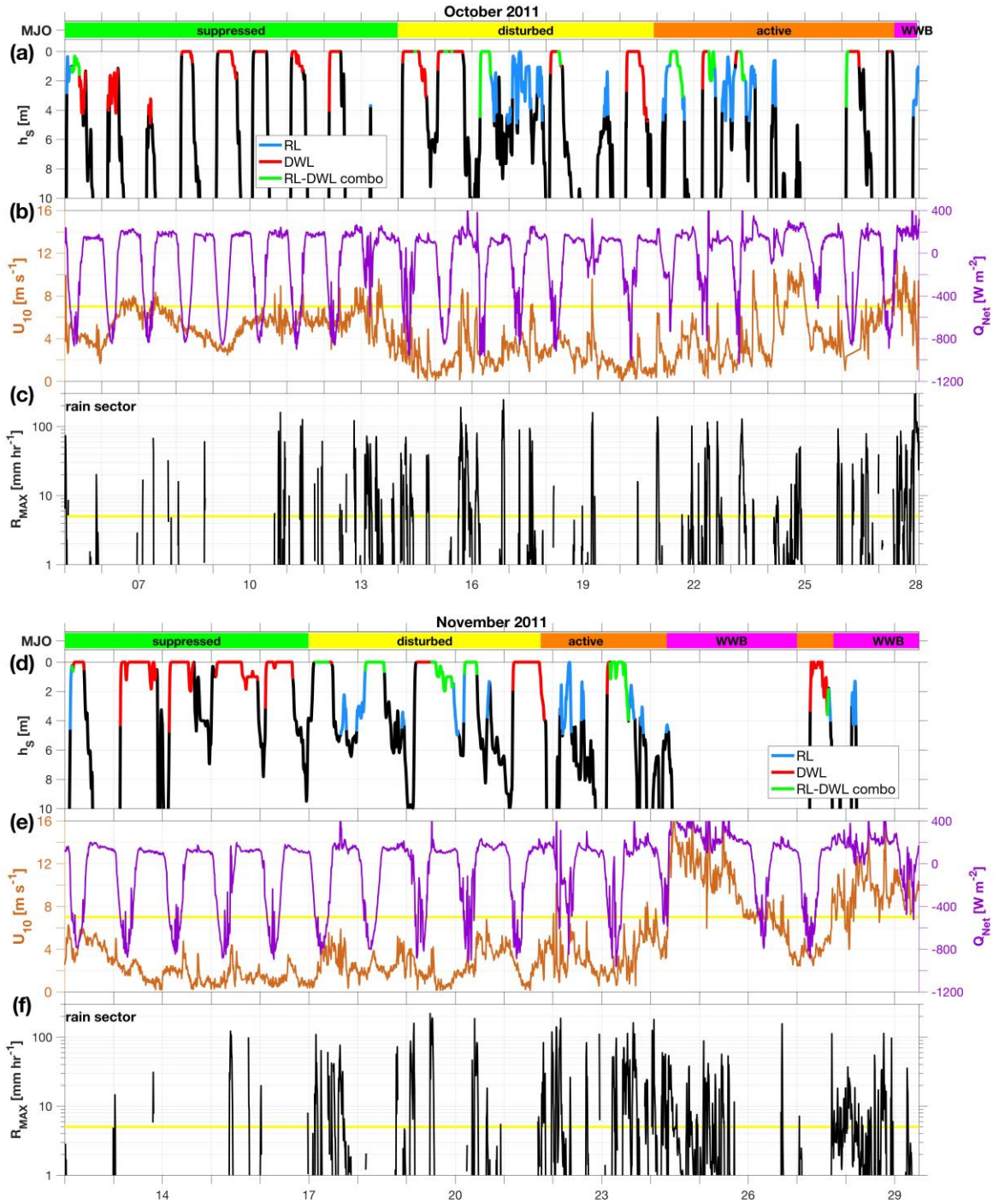
1259

Figure 4: Histograms of observed central Indian Ocean: (a) stable layer depth, h_S ; (b) stable layer thickness, $h_B - h_S$; (c) thermocline depth, h_{TC} , normalized by length of dataset.



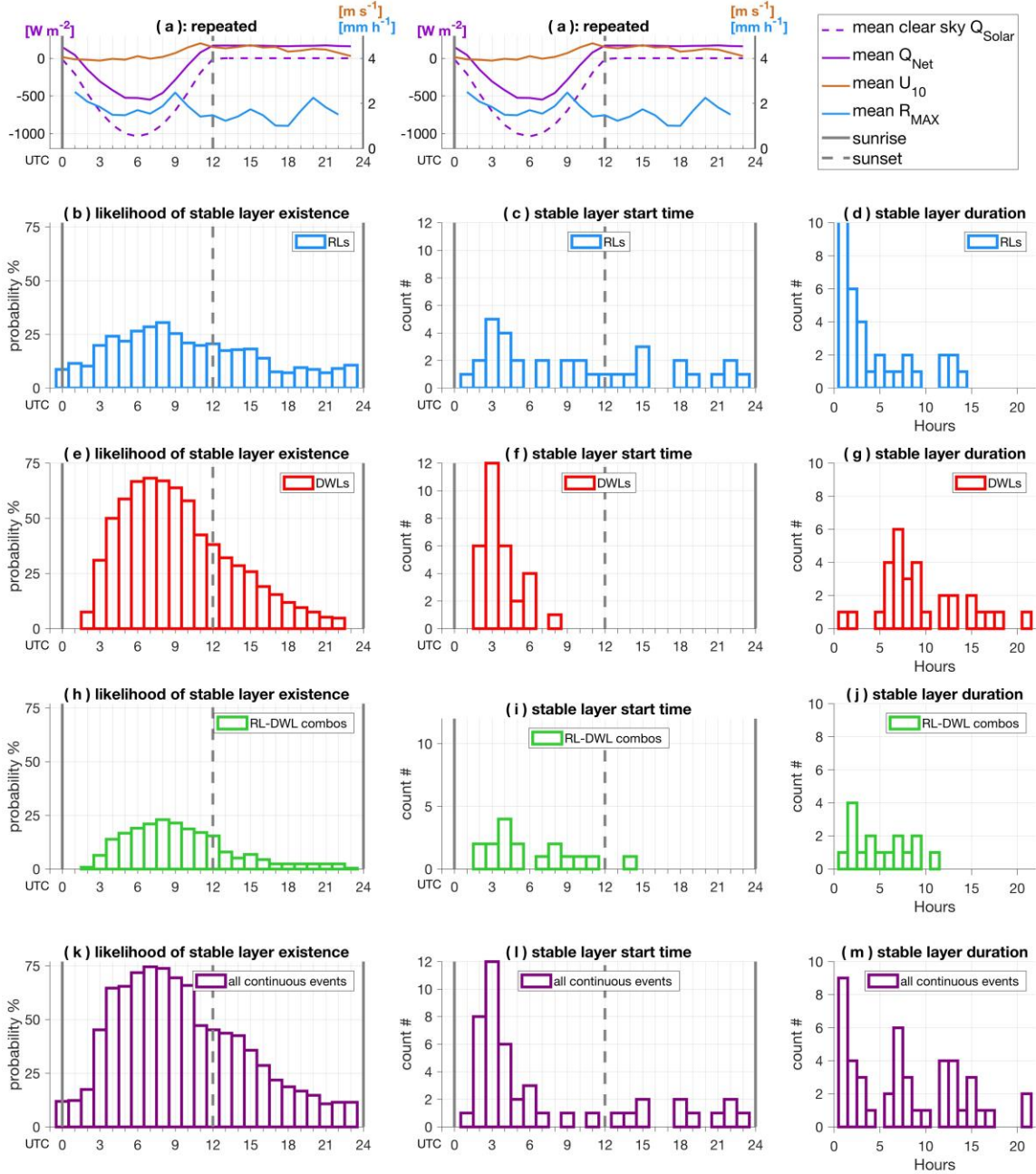
1260
 1261
 1262
 1263
 1264

Figure 5: Histogram of U_{10} measured during DYNAMO for different 0-5 m ocean stability conditions: all data (grey), when no stable layers were present (i.e. when water was well-mixed from 0-5 m, black), when only DWLs were present (red), when RL-DWL combination layers were present (green), and when only RLs were present (blue).



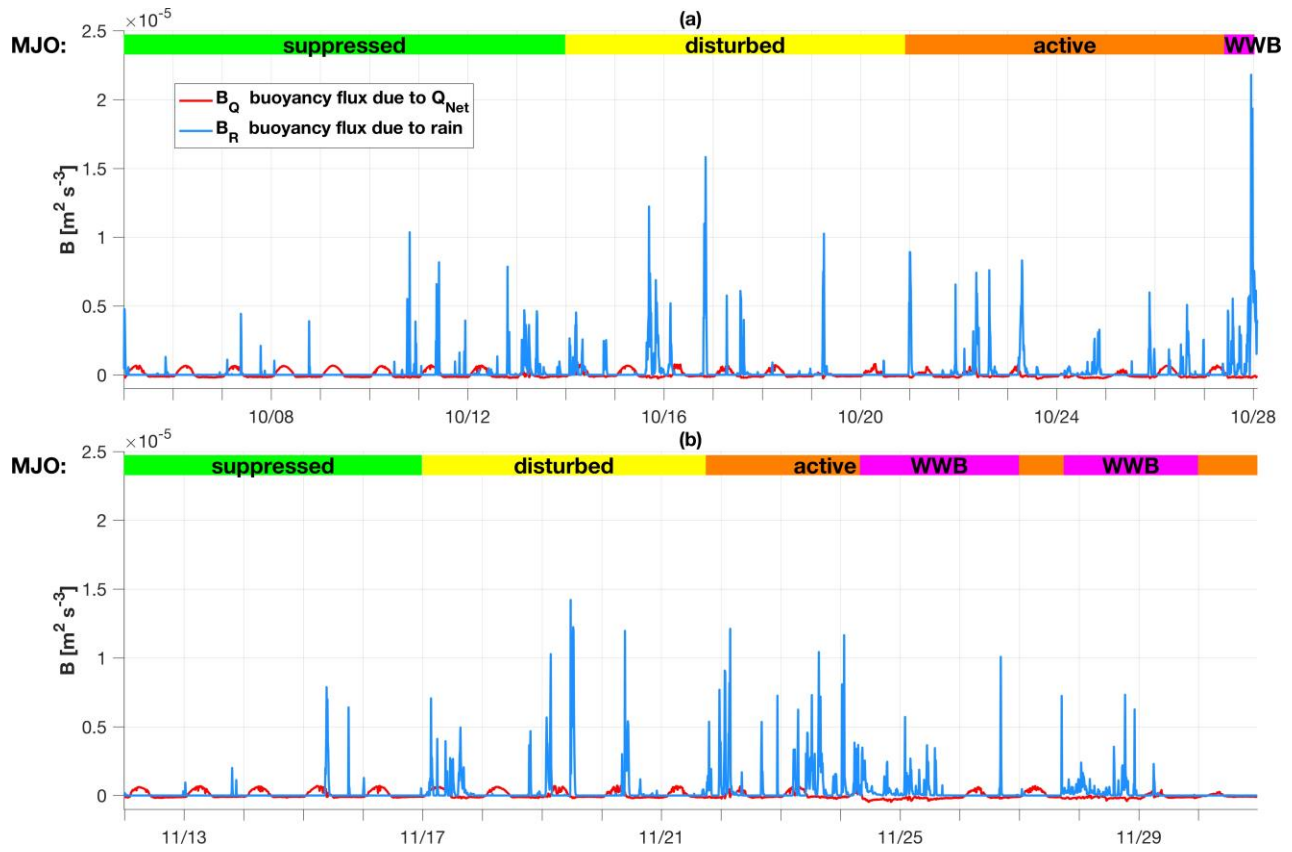
1265
 1266
 1267
 1268
 1269
 1270
 1271
 1272

Figure 6: Time series of observed ocean stable layer depth, h_s , colored by stable layer type (a, d); U_{10} and Q_{Net} (b, e); max R observed within the radar rain sector and the ship gauge, R_{MAX} (c, f). Yellow horizontal lines denote $U_{10} = 7$ m s⁻¹ and $Q_{Net} = -500$ W m⁻² in (b, e) and $R_{MAX} = 5$ mm h⁻¹ in (c, f).



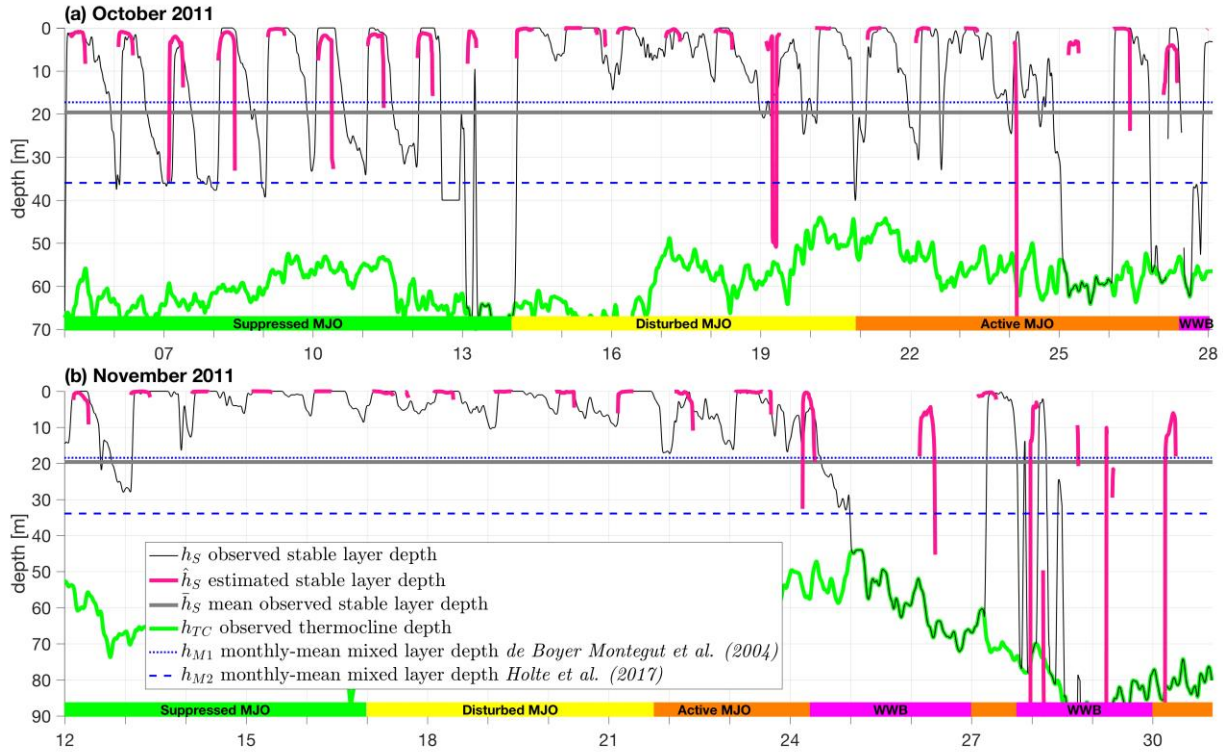
1273
1274

1275 **Figure 7:** Hourly means of clear sky Q_{Solar} , Q_{Net} , U_{10} , R_{Max} (a) repeated in both top panels for
1276 reference. Hourly likelihood of stable layer existence (b, e, h, k), counts of stable layer start
1277 times (c, f, i, l); counts of stable layer durations (d, g, j, m), of all RLs, all DWLs, RL-DWL
1278 combinations, and all continuous stable layers regardless of type. The RL and DWL categories
1279 include instances of RL-DWLs, in which RLs and DWLs overlapped. The “all continuous stable
1280 layer” category in (k, l, m) considers a time period in which multiple stable layers occurred as
1281 one event, so the upper panels do not add to the bottom panel. Top panels: mean diurnal cycles
1282 of clear-sky Q_{Solar} , Q_{Net} , U_{10} , and R_{MAX} . In this study, sunrise = 00:30 UTC (vertical solid line)
1283 and sunset = 12:30 UTC (vertical dashed line), which are marked in the 0th and 12th histogram
1284 bins.



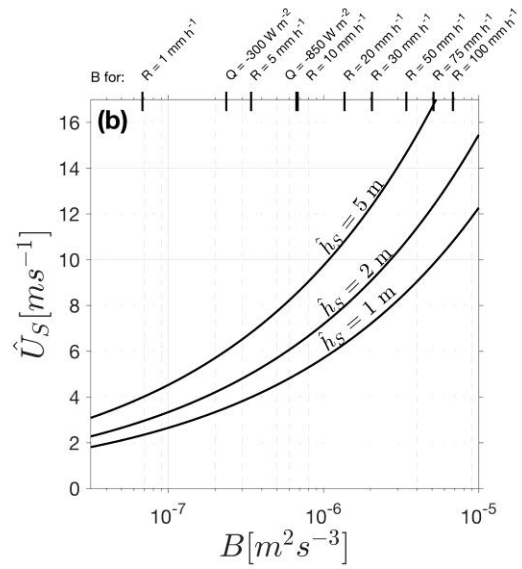
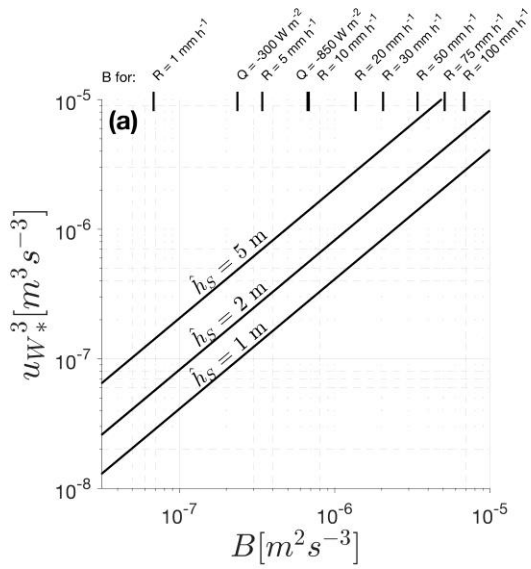
1285
 1286
 1287
 1288
 1289

Figure 8: DYNAMO measured buoyancy flux, B , due to heating, cooling, and evaporation by Q_{Net} , B_Q , and due to the net effect of rain freshening and rain cooling, B_R (**Appendix A**)



1290
 1291
 1292
 1293
 1294
 1295
 1296

Figure 9: DYNAMO observed stable layer depth (h_S), estimated stable layer depth from surface fluxes (\hat{h}_S), mean observed stable layer (\bar{h}_S), observed thermocline depth (h_{TC}), and monthly-mean mixed layer depths (h_{M1} and h_{M2}) for this location in Oct and Nov 2011 according to climatologies by *de Boyer Montegut et al. (2004, h_{M1})* and *Holte et al. (2017, h_{M2})*. Note: different y-axis scales in each month.

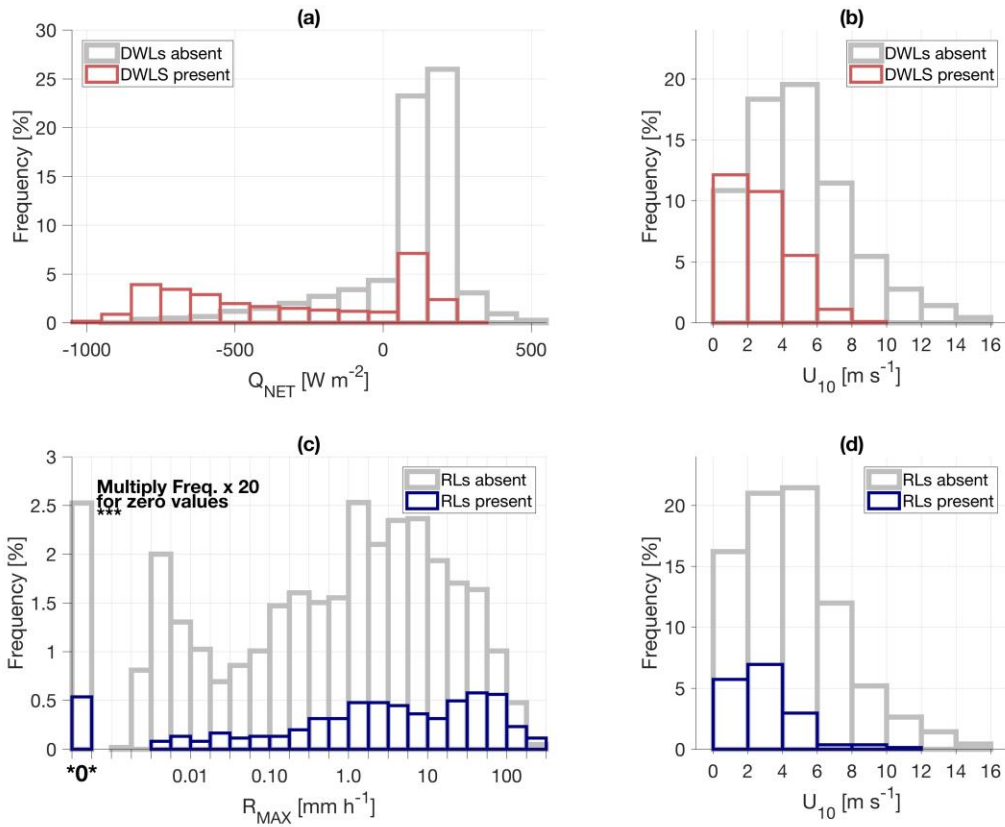


— u_{W*}^3 calculated with measured B and constant \hat{h}_S [7]

— \hat{U}_S calculated with measured B and constant \hat{h}_S [10]

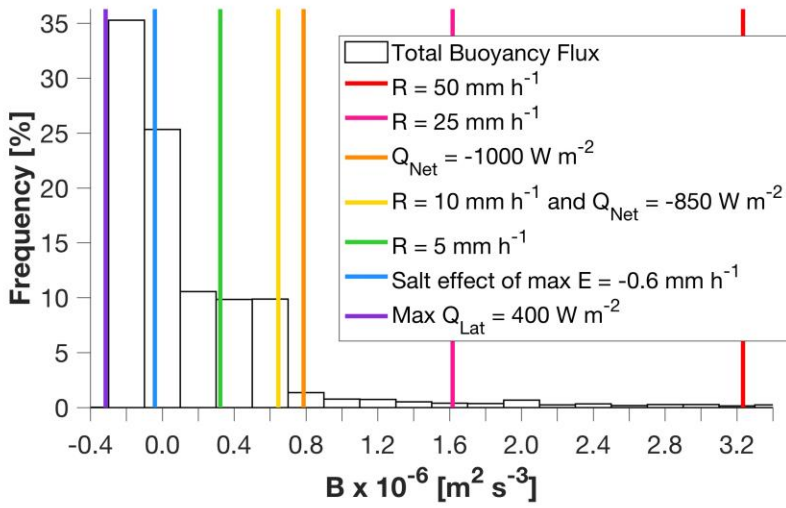
1297
1298
1299
1300
1301
1302
1303
1304

Figure 10: Calculated (a) u_{W*}^3 and (b) \hat{U}_S using different stable layer depths of $h_s = 1, 2,$ and 5 m and measured B in [7] and [10]. The value of \hat{U}_S is the highest value of U_{10} at which wind mixing and B should support the existence of a stable layer at depth h_s . Examples of B for various net heat fluxes (Q_{Net} abbreviated as Q in plot) and rain rates (R) shown atop each plot for reference.



1305
 1306
 1307
 1308
 1309
 1310

Figure 11: Histograms of Q_{NET} , U_{10} , and R_{MAX} (max R observed within rain sector of **Fig. 1**) in either the absence or presence of DWLs (a, b) or RLs (c, d) normalized by length of dataset.



1311
 1312 **Figure A1:** Normalized histograms of measured central Indian Ocean buoyancy flux, B . Vertical
 1313 colored lines indicate B for various heat fluxes (negative into the ocean), rain rates, and
 1314 evaporation.